

Stress-driven photo-reconfiguration of surface microstructures with vectorial light fields

I Komang Januariyasa,¹ Francesco Reda,¹ Nikolai Liubimtsev,² Pawan Patel,^{2,3} Cody Pedersen,⁴ Fabio Borbone,⁵ Marcella Salvatore,¹ Marina Saphiannikova,^{2,3,*} David J. McGee,^{4,*} and Stefano Luigi Oscurato^{1,*}

¹Physics Department “E. Pancini”, University of Naples Federico II, Complesso Universitario di Monte Sant’Angelo, via Cinthia, 80126, Naples, Italy.

²Division Theory of Polymers, Leibniz Institute of Polymer Research Dresden, 01069 Dresden, Germany.

³Faculty of Mechanical Science and Engineering, Dresden University of Technology, 01062 Dresden, Germany

⁴Department of Physics, The College of New Jersey, Ewing, New Jersey 08628, USA.

⁵Department of Chemical Sciences, University of Naples “Federico II”, Complesso Universitario di Monte Sant’Angelo, Via Cintia, 80126 Naples, Italy.

*Stefano Luigi Oscurato, e-mail: stefanolugi.oscurato@unina.it

*Marina Saphiannikova, e-mail: grenzer@ipfdd.de

*David J. McGee, e-mail: mcgeed@tcnj.edu

Abstract

Pattern formation driven by mechanical stress plays a fundamental role in shaping structural organization in both natural and human-made systems. However, achieving localized and programmable control of individual microstructures remains a challenge. Here, we present a vectorial field-guided lithography as a novel and versatile method for the photo-reconfiguration of photosensitive azopolymer microstructures. Building on the Viscoplastic PhotoAlignment model, recently proposed to describe the stress-driven response of azomaterials, we reveal structured polarization fields that are directly mapped into programmable surface architectures through stress-driven deformation. Using a digital polarization rotator implemented via a spatial light modulator, we prove the single-step fabrication of anisotropic, bent, and chiral microstructures from a single pre-

patterned geometry, highlighting the power of polarization vector fields as active design parameters. Experimentally, we validate the theoretical model and demonstrate its predictive strength even under fully structured light, establishing for the first time a comprehensive theoretical framework capable of quantitatively designing target morphologies. Our work demonstrates that the full vectorial nature of light, and not just its intensity, can dictate the mechanical reshaping of functional polymer surfaces, providing a new platform for the programmable design of complex micro-architectures with applications in photonics, microfluidics, and biology.

Introduction

Stress-driven pattern formation is a fundamental mechanism that governs the emergence of complex structures across spatial and temporal scales in both natural and engineered systems. On Earth's surface, tectonic stress sculpts mountains and fault lines.¹ In living organisms, differential growth induces mechanical instabilities, leading to the characteristic folds of the human brain,² the wrinkling of the skin,³ and the morphological features in plant leaves.⁴ Even at the microscopic level, bacterial colonies self-organize into complex morphologies under the influence of mechanical stress.⁵ Despite their diverse origins, these systems share a common underlying principle. When internal stress accumulates, the system undergoes morphological reorganization to minimize free energy, often through symmetry breaking, giving rise to structured topographies. Inspired by this universal process, the engineering of controlled stress-driven deformations has emerged as a powerful strategy to design functional surfaces. Examples include tunable wrinkling in soft materials,⁶ origami-inspired folding,⁷ and buckling of stretchable materials.⁸

All of these examples leverage the relationship between a triggering external action and the stress generated within the material, with this interaction guiding the material into forming structures. Typically, these systems harness the stress induced by external stimuli such as temperature, humidity, or mechanical load.^{9,10} Light, which allows remote, non-contact control with high spatial and temporal accuracy, offers distinct advantages among the others stimuli.^{11,12} More importantly, light inherently carries vectorial information through its polarization state, a degree of freedom that remains largely untapped for stress-driven surface structuring and light-based photopatterning processes such as standard optical lithography.

Amorphous azobenzene-containing polymers (referred to as azopolymers), with their unique light-induced anisotropic stress-driven deformation, offer a route to bridge this gap and harness the vectorial nature of light for surface patterning.^{13–15} Key elements for this process are the photochemical properties of the azobenzene chromophores embedded in the hosting polymeric

material matrix. Following cyclic *trans-cis* photoisomerization with UV/visible light, the azobenzene molecules reorient perpendicular to the direction of the local light polarization,^{13,14} transferring their alignment to the polymer to which they are attached through either covalent^{16,17} or supramolecular interactions.^{18,19} The mechanical stress resulting from the photoalignment is relieved by directional plastic deformation of the material in the irradiated area.^{17,20} When the azopolymer is prepared as a thin film, this light-induced phenomenon directly produces relief patterns on the free surface of the film. The morphology of such reliefs reflects the local geometry of the incident vectorial light field, showing a dependence on both the spatial intensity distribution^{21–24} and its local polarization state.^{25–28} Empirical and phenomenological exploitation of the vectorial nature of the light-induced surface deformation of azopolymers has been used to fabricate a wide range of different surface relief architectures. Interestingly, complex anisotropic microstructures, with tailored morphology even in three dimensions, can also be obtained when the intensity or the polarization of the incident light is used to reconfigure the geometry of already pre-patterned surfaces. Complex isometric,²⁹ and strongly unidirectional^{30–32} and bidirectional^{33–35} anisometric architectures have been achieved from pristine arrays of azopolymer micropillars in this scheme.

The modeling of azopolymer photopatterning processes has been a long-standing challenge due to the complex interplay between light parameters and material response.¹⁴ However, a recent theoretical framework, the Viscoplastic PhotoAlignment (VPA) model, has been proposed to describe the process as a unique stress-driven vectorial phenomenon initiated by the light. This picture could ultimately bridge the existing gap between the nanoscopic photomechanics of azobenzene molecules and the resulting macroscopic surface relief geometries.¹⁷ Beyond rationalizing the complex multiscale photoinduced dynamics in these materials, the relevance of this model lies in the possibility of finally having predictive and inverse design capabilities for the surface reliefs on azomaterials. In addition, the validation of the model in the general case of irradiation with structured vectorial light fields could provide foresight for the design of unconventional illumination schemes and materials for new lithographic processes.

In this work, we demonstrate a new level of stress-driven morphological control based on the programmable photo-reconfiguration of pre-patterned azopolymer surfaces using structured vectorial light fields. Specifically, we analyze the photo-reconfiguration of azopolymer micropillars illuminated by spatially varying polarization patterns, which are generated by a digital polarization rotator implemented via a computer-controlled spatial light modulator.^{36,37} This optical system offers large flexibility in the polarization pattern design, making our configuration a prototype of a more general vectorial field generator able to control the stress-driven morphological deformation of the azopolymers. Furthermore, our experimental framework provides an ideal test ground to further

validate the VPA model for arbitrary structured light. The combined experimental and theoretical study presented here demonstrates unprecedented quantitative predictive capabilities on the morphology and the stress-driven deformation dynamics of complex azopolymer microstructures. Our results establish the concept of the vectorial field-guided lithography, summarized in Fig. 1, where a rationally designed vectorial light pattern is directly mapped into programmable microstructure morphologies mediated by tailored light-induced stress pathways. The presented framework opens up the exploration of vectorial external stimuli as a tool for shaping even diverse material systems, paving the way for applications in different fields such as photonics, microfluidics, and biology.

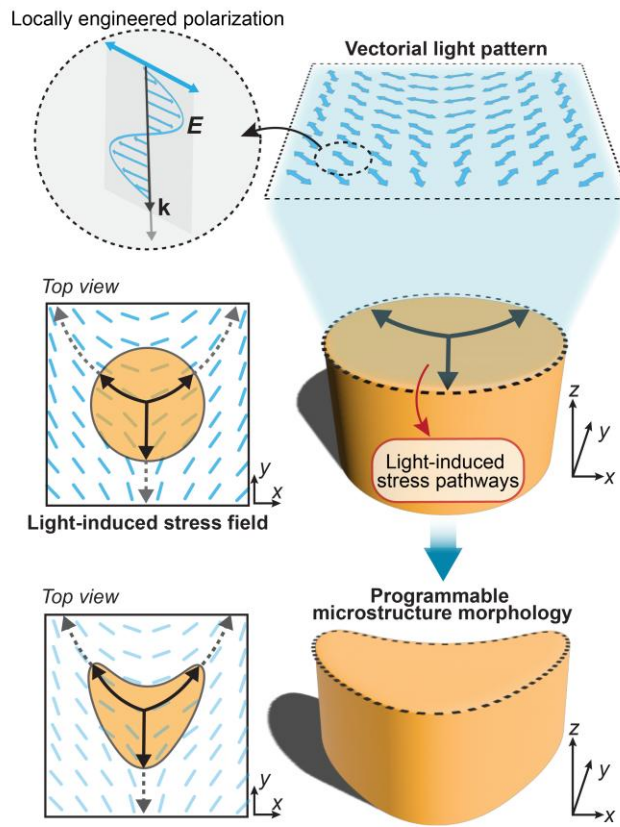


Fig 1. Concept of vectorial field-guided photo-reconfiguration of azomaterial microstructures. A vectorial light field with locally engineered linear polarization directions (first row) is irradiated onto the top surface of a cylindrical micropillar, inducing stress pathways (black arrows in the middle row). Their directions depend on the light field distribution (dashed blue lines) and guide the anisotropic structural deformation of the illuminated micropillar along the same directions (bottom row).

Results

1. Stress-driven morphological deformations from linearly polarized light

As a foundational step of this work, we first revisit the photomechanical response of azopolymer micropillars to uniform linearly polarized light. This typical photo-reconfiguration scenario,^{31,35} schematized in Fig. 2a, has been previously used to empirically induce directional small, reversible deformations³⁸ and, in some cases, complete remorphing of azopolymer micropillar arrays.³⁹

For our analysis, the azomaterial surface is designed as an array of cylindrical micropillars and placed in the x-y plane. The surface photo-deformation involves illumination with a homogenous laser beam, which in our scheme is linearly polarized along the x-axis. The polarization direction is indicated by the blue arrow identifying the direction of electric field (\mathbf{E}) in Fig. 2a. A uniform intensity distribution is taken into account here to minimize contributions from intensity gradients, which are known to be an additional relevant mechanism driving surface deformation in azopolymer films^{21,22} and microstructures.⁴⁰ Moreover, the uniform illumination also ensures that each micropillar within the irradiated region experiences the same photo-deformation dynamics.

Fig. 2b shows the Scanning Electron Microscopy (SEM) images of our fabricated pristine structured surface. For the photo-reconfiguration experiment, a linearly polarized laser beam at a wavelength of 488 nm, was used. The beam was sufficiently expanded to ensure spatial uniformity of the intensity in the illuminated area. Details on our azopolymer, the preparation and the geometry of the pre-patterned array, and the optical setup are presented in Materials and Methods and in Fig. S1-S2-S3. Fig. 2c shows the reconfiguration process of a micropillar in the array achieved by exposing the surface for 18 minutes to a laser intensity of 160 mW/cm². According to the expected phenomenology,³¹ the irradiation breaks the symmetry of the initially isotropic cylindrical micropillar, resulting in an elongated microstructure in the direction of the polarization of the incident light beam. The same happens for all the micropillars in the homogeneously illuminated area.

Our first goal is to conceptualize such phenomenology within the stress-driven morphological deformation framework of the VPA model. The amorphous polymer in the model is schematized as a series of rod-like polymer backbone segments, to which the azobenzene chromophores are attached as side chains, preferentially at right angles. The directional photo-deformation of the azopolymer arises from the light-induced reorientation of the azobenzene chromophores in the direction perpendicular to the electric field \mathbf{E} . Consequently, the illumination tends to align the polymer backbones along the polarization direction (Fig. 2d).^{17,20} In this process, the electric field vector \mathbf{E} of the homogeneously polarized beam plays the role of a nematic director, breaking the symmetry of the initially isotropic molecular system.¹⁴

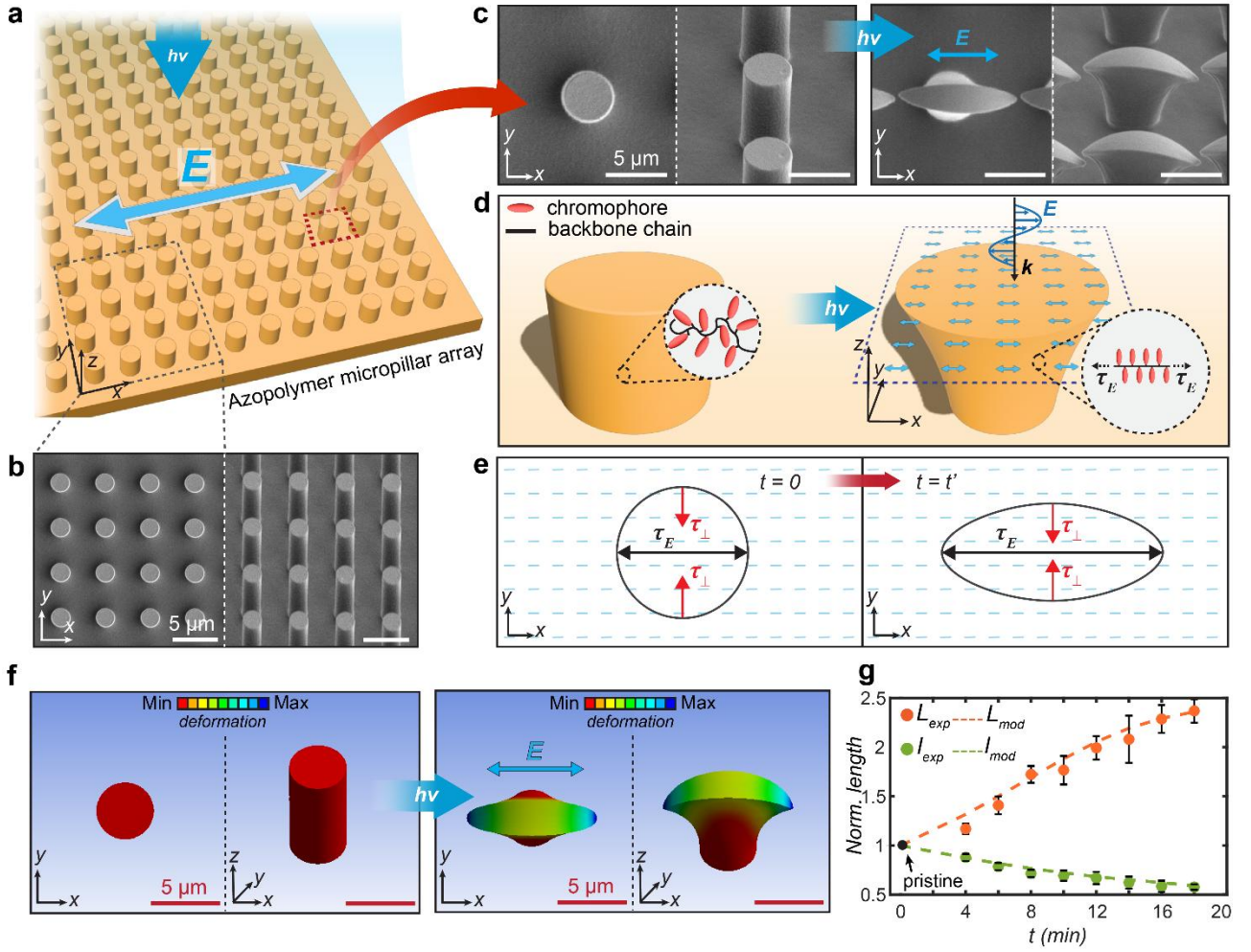


Fig 2. Encoding of polarization direction to morphological anisotropy. **a)** Illumination scheme of homogenous linearly polarized beam onto an azopolymer micropillar array. **b)** SEM images of the pristine state of the micropillar array from top (left) and tilted (right) views. **c)** SEM images of a single pristine micropillar from top and side views (left) and of an anisotropically deformed micropillar resulting from illumination with uniformly polarized light. **d)** Illustration of the relationship between molecular photoalignment and the micro-scale photo-deformation. **e)** Scheme of the emerging stress induced by the photoalignment at the very initial stages of illumination ($t = 0$) and after a certain exposure time ($t = t'$). The tensile stress (τ_E) and the compressive stress (τ_{\perp}) are parallel and orthogonal to the polarization direction, respectively. **f)** VPA modeled morphological evolution of the azopolymer micropillar (top and tilted view) corresponding to the experimental results in panel b). The colormap represents vertical displacement: red corresponds to the initial state, while dark blue indicates the maximum downward displacement. **g)** Dynamic evolution of the experimental and modeled deformation of the micropillars. L_{exp} , l_{exp} , L_{mod} , and l_{mod} represent the major axis and minor axis values of the top surface, experimentally measured and modelled, respectively. The geometrical parameters have been normalized by the diameter (D_0) of the pristine micropillar. Error bars indicate the standard deviation of 16 measured pillars in the array for each exposure time.

The complete formalism linking the kinetic equations of azobenzene isomerization to the stress induced in the polymer is detailed in the Supplementary note 1. To emphasize the most relevant aspect of the model for this work, we present here a simplified expression that directly relates the light-induced stress tensor $\boldsymbol{\tau}$ to the polarization direction $\hat{\mathbf{E}}=\mathbf{E}/|\mathbf{E}|$ of the homogeneous linearly polarized beam. This simplified equation can be written as:

$$\boldsymbol{\tau} = \tau_0(\hat{\mathbf{E}}\hat{\mathbf{E}} - \boldsymbol{\delta}/3). \quad (1)$$

In this relation, τ_0 is the magnitude of the stress, which is proportional to the light intensity,⁴¹ the dyadic product $\hat{\mathbf{E}}\hat{\mathbf{E}}$ is a tensor that contains the information about the principal axes of stress tensor, and $\boldsymbol{\delta}$ is the unit tensor. This relation was derived assuming an initial isotropic state of the polymer backbones and is valid for the initial stages of irradiation. The main feature emerging from Equation (1) is that the major principal axis of the stress tensor for linearly polarized light is aligned with the local director $\hat{\mathbf{E}}$, whose uniform spatial distribution is represented by the blue segments in Fig. 2e. In particular, for the linear polarization $\hat{\mathbf{E}} = (1,0,0)$ aligned with the x-axis, $\boldsymbol{\tau}$ explicitly becomes:

$$\boldsymbol{\tau} = \tau_0 \begin{pmatrix} 2/3 & 0 & 0 \\ 0 & -1/3 & 0 \\ 0 & 0 & -1/3 \end{pmatrix}. \quad (2)$$

According to equation (2) the stress tensor is represented by three principal normal stresses: the tensile component $\tau_E = 2\tau_0/3$ acting along the major principal direction (x-axis here), and the compressive components $\tau_{\perp} = -\tau_0/3$ acting in the two perpendicular minor principal directions (Fig. 2e).⁴² Such a light-induced stress tensor leads to the uniaxial elongation of the illuminated azopolymer along the local light polarization direction and to the compression along the orthogonal directions. Following this description, the stress field of a uniform polarization pattern can be illustrated as a single stress pathway (the black arrow in Fig. 2e), corresponding to the major principal direction of the system, along which the polymer deformation mainly occurs.

It is worth noting that the results of the VPA model apply to any polarization state of the irradiated field. In particular, for an elliptically polarized light, relation (1) predicts a general biaxial deformation of the azopolymer micropillar, where two principal stress directions correspond to the axes of the light polarization ellipse.^{43,44}

To model the micropillar photo-deformation in the situation of Fig. 2, we performed finite element simulations using the complete VPA model (Supplementary note 1), where the azopolymer is treated as a viscoplastic material, and the light-induced stress field was implemented via a custom subroutine in ANSYS software (see Materials and Methods). Fig. 2f shows the modeled initial azopolymer microstructure and its morphology at the end of the photo-deformation process. The anisotropic

microstructure that results from the VPA model is clearly in excellent agreement with experimental micropillars in Fig. 2c.

To further investigate the agreement beyond just the morphology at the final stages of the reconfiguration process, we analyzed the temporal dynamics of the azopolymer photo-deformation, extracted from the characterization of the microstructure morphology at different exposure times. The micropillar deformation, both in experiments and model, is quantitatively described by measuring the major (L) and the minor (l) axis of the pseudo-elliptical shape of the top surface, respectively. Both parameters were normalized to the diameter (D_0) of the pristine circular micropillar profile before exposure (see also Movie S1 and Fig. S4 for dynamic modeled and experimental evolution, respectively). The comparison, reported in Fig. 2g, demonstrates quantitative agreement at each stage of the deformation process.

2. Programmable optical field-guided deformations

The analysis conducted above for the uniform linear polarization state allows us to extend the established concept of the uniform stress pathway of the VPA model to the description of deformation induced by vectorial polarization states. We limit our treatment to spatially structured patterns of linear polarization, but the results are generalizable to arbitrary polarization states. Namely, according to Equation (1), when the polarization field is spatially structured, (i.e. $\mathbf{E} = \mathbf{E}(\mathbf{r})$) the stress field also becomes spatially varying ($\boldsymbol{\tau} = \boldsymbol{\tau}(\mathbf{r})$). In this condition, at each point \mathbf{r} within the irradiated azopolymer, the local major principal axis of the stress aligns with the direction of the local linear polarization, enabling a spatially controlled deformation ultimately directed by the optical field.

The vectorial dependence of the stress-driven deformation can be easily visualized through the array of azopolymer micropillars, illuminated with discretized structured patterns of linearly polarized light. In this configuration, each microstructure in the array is deformed according to the local linear polarization direction, acting as a morphological polarization sensor. For our experiments, we used a digital polarization rotator based on a Spatial Light Modulator (SLM) to irradiate the pre-patterned azopolymer micropillar array. This optical system is designed to rotate the azimuth angle φ of a linearly polarized beam and consists of an SLM interposed between two quarter-wave plates whose axes are each oriented at $\pm 45^\circ$ with respect to the incident linear polarization (see Materials and Methods).^{19,37} The output polarization angle φ is determined by the phase delay introduced between the two orthogonal components of the circularly polarized light incident on the device, according to the gray level of a computer-generated image displayed on the SLM (see also Fig. S5).^{25,27} The digital image can be designed to create spatially varying maps $\varphi = \varphi(x, y)$ of linear polarization by assigning an independent gray value to each pixel of the SLM, as schematically shown in Fig. 3a.

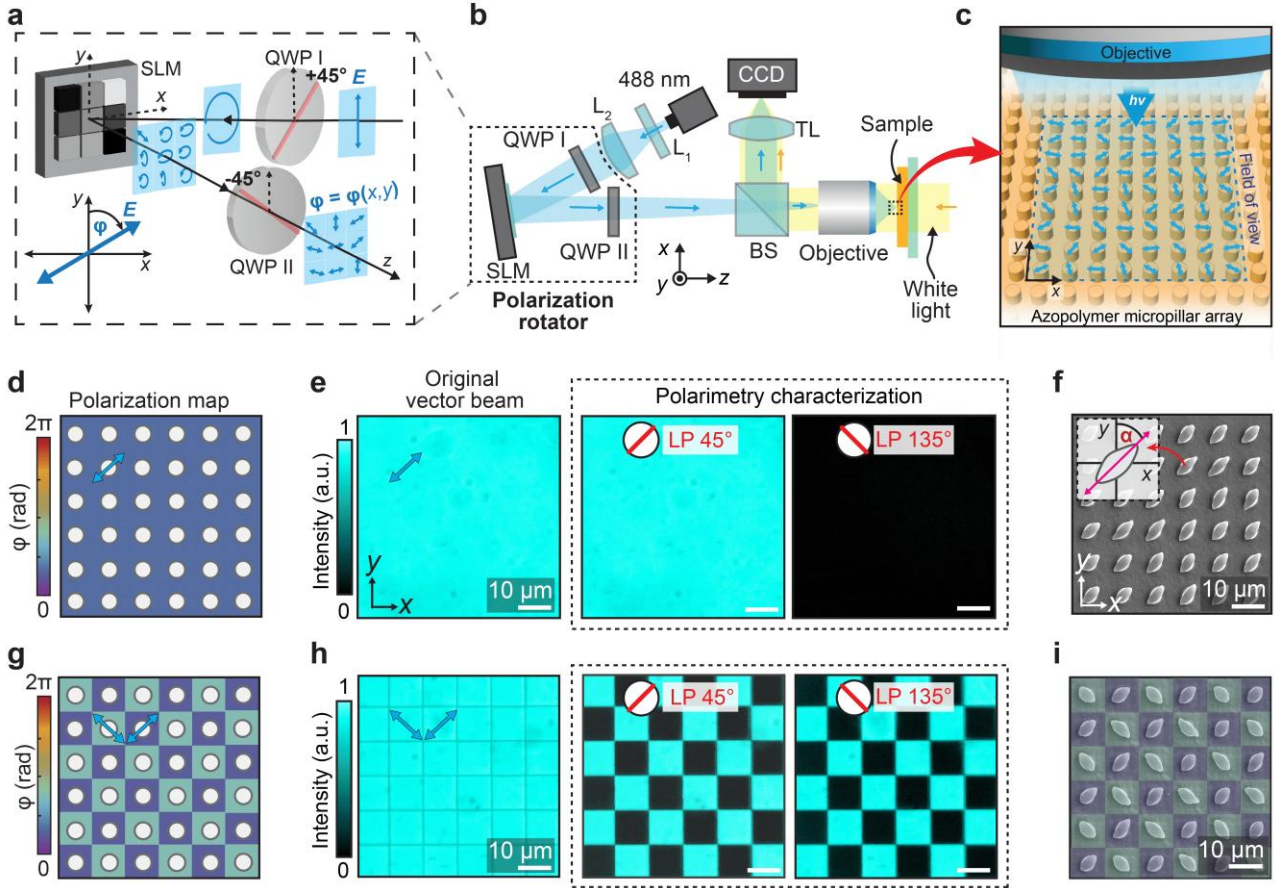


Fig 3. Generation of engineered vector beam and spatial anisotropic control of the photo-deformation.

a) Working principle of a digital polarization rotator: a plane wave input with linear vertical polarization first passes through a first quarter waveplate (QWP I) with its fast axis at $+45^\circ$ (relative to the y -axis), is reflected by a spatial light modulator (SLM), and passes through a second quarter waveplate (QWP II) whose fast axis is oriented at -45° (relative to the y -axis). The output beam exhibits a spatially modulated linear polarization. The polarization azimuth angle φ is defined as the angle between the polarization direction and the y -axis along the clockwise rotation direction. **b)** Optical setup scheme. The digital polarization rotator is integrated into a projection system that directs the illumination onto the azopolymer micropillar surface using a 40X objective. White light propagating from the back of the sample, and a CCD camera are used to observe the surface of the sample. **c)** Illustration of the projected spatially-varying vector beam on the micropillar array. **d)** Uniform polarization map designed at $\varphi = +45^\circ$. **e)** Experimental confirmation of the targeted polarization state designed in **d)**. The optical intensity image of the irradiated light pattern is collected at the sample plane. The optical images related to the polarimetry characterization are collected after a linear polarizer with the polarization axis set to 45° (left), and 135° (right). **f)** SEM image of the deformed micropillar after the exposure with the light pattern shown in **e)**. **g)** Polarization map of checkboard polarization pattern designed with $\varphi_1 = +45^\circ$ and $\varphi_2 = -45^\circ$. **h)** Experimental confirmation of the targeted polarization state designed in **g)** as described for panel **e)**. **i)** SEM image of the deformed micropillar after the exposure with the light pattern shown in **h)**.

For the 256 gray levels addressable to our SLM (8-bit images), the achievable angular resolution in the output polarization angle is $\sim 1.4^\circ$, which allows fine control over the polarization orientation across the beam profile. In our experimental setup (Fig. 3b), the digital polarization rotator was

integrated into an optical projection system (see Materials and Methods for further details) to initiate the photo-deformation process of the azopolymer micropillar arrays with spatial selectivity (Fig. 3c). Such an optical configuration enables selective, site-specific remorphing of micropillars across the sample with polarization-dependent individual tuning.

Fig. 3d-f first demonstrate the ability of this system to replicate the experimental case presented in the previous section for homogeneous micropillar photo-deformation along on-demand directions. For this experiment, we targeted a uniform linear polarization illumination with an azimuth angle $\varphi = +45^\circ$ across the entire field of view of the system (approximately $130\ \mu\text{m} \times 78\ \mu\text{m}$, see also Materials and Methods). To enhance visualization here and in the remainder of this paper, we use a violet-to-red colormap to directly represent the designed polarization maps. The colors encode the polarization angle φ emerging from the digital rotator system for each gray value addressed to the SLM according to the measured calibration curve reported in Fig. S5. Within this representation, the uniform polarization pattern for $\varphi = +45^\circ$ appears as the homogenous blue color in Fig. 3d.

Fig. 3e shows the experimental optical images representing the irradiated homogenous light pattern, together with a polarimetry characterization confirming the achievement of the targeted polarization state as outcome of the digital polarization rotator. It should be mentioned that, for the only sake of improving the visualization, the optical images in Fig. 3 were collected through a CCD camera using an incoherent LED at 477 nm (with full-width-half-maximum of 29 nm) as a light source. In this way we could drastically reduce unwanted interference fringes caused by the coherent 488 nm laser source used in the photo-reconfiguration experiments (see Materials and Methods), without affecting the main outcomes of the characterization of the digital polarization rotator system.

As expected from the previous analysis, a homogeneous elongation of all illuminated micropillars in the direction of the linear polarization was obtained in the experiment (Fig. 3f, and Table S1), with a measured average orientation angle $\alpha = +43^\circ \pm 5^\circ$, in full agreement with the target design.

We now demonstrate the next level of control enabled by our optical configuration, where spatially varying polarization maps can be designed to individually reshape the micropillars with independently engineered orientation α across the entire field of view. Owing to the square lattice arrangement of the micropillars in our array, the optical field of view can be easily segmented into square regions, each targeting an individual micropillar with a specific linear polarization orientation (see Materials and Methods). The polarization map in Fig. 3g was designed as a checkerboard pattern of linearly polarized light oriented at alternating orthogonal azimuth angles of $\varphi_1 = +45^\circ$ and $\varphi_2 = -45^\circ$. Similarly to the previous uniform illumination, the optical images of the irradiated homogeneous light pattern, together with polarimetry characterization confirming the alternating targeted polarization state, are shown in Fig. 3h. In the image of the irradiated field (first image in

Fig. 3h), distinct dark lines are visible at the edges of each of the square regions, as expected from the emergence of singularities at positions of sharp polarization variations in the optical wavefield.⁴⁵ These field discontinuities provide additional evidence of the system's ability to control vectorial light. However, they do not play a role in this photo-reconfiguration experiment as they are located outside to the targeted azopolymer micropillars.

The irradiation of the checkerboard polarization pattern on the azopolymer array resulted in the stress-driven regular reshaping of the micropillars, with alternating photo-deformation orientations measured from the SEM image (Fig. 3i) of $\alpha_1 = +43^\circ \pm 4^\circ$ and $\alpha_2 = -43^\circ \pm 5^\circ$, in full agreement with the designed polarization map. Additional experimental examples, highlighting the flexibility of the optical system and the peculiar alternating surface patterns achievable through the stress-driven photo-reconfiguration of this square micropillar array and the possibility to achieve progressive linear rotations, are shown in Fig S6 and S7, respectively.

To conclude with this section, it is worth highlighting that the framework proposed here can be further extended to enable coupled modulation of both light intensity and polarization by introducing an additional linear polarizer into the optical setup, as illustrated in Fig. S8-9. This extension provides the capability to simultaneously control both the pillar elongation direction (polarization) and the deformation strength (intensity) and could represent a first prototype of a full vectorial lithography able to achieve arbitrary complex directional patterns on surfaces.

3. Stress-driven complex microstructures from vectorial field

Beyond piece-wise spatial selectivity across the sample, we explore now the regime of complex programmability of individual microstructures through locally engineered stress pathways originated by high-resolution structured polarization fields.

Fig. 4a shows the principle underlying the design of this photo-reconfiguration scheme. Due to the high density of addressable pixels in the optical pattern projected onto the azopolymer surface (~ 15 pixels per μm), we can design high-resolution polarization maps that vary spatially across the surface of a single micropillar (diameter of $D_0 = 6.7 \mu m$ for these experiments, see also Materials and Methods). According to the VPA model, each volume element dV of the irradiated azopolymer would experience the effect of the stress field generated by the local polarization state of the light (Fig 4a), tending to deform along the major principal direction of the maximum tensile component (with the same phenomenology described in Fig. 2). To have distinct directional deformations, adjoining volume elements should deform along closely varying directions that are only slightly different. This requires that the orientation $\varphi(x, y)$ of the light polarization field, which dictates the major principal stress direction (see also Supplementary note 2 and Fig. S10), varies smoothly across

the x-y plane, as shown in Fig. 4a. In this condition, locally curved stress pathways emerge (black lines in Fig. 4b), which lead to complex deformation geometries for the azopolymer microstructures.

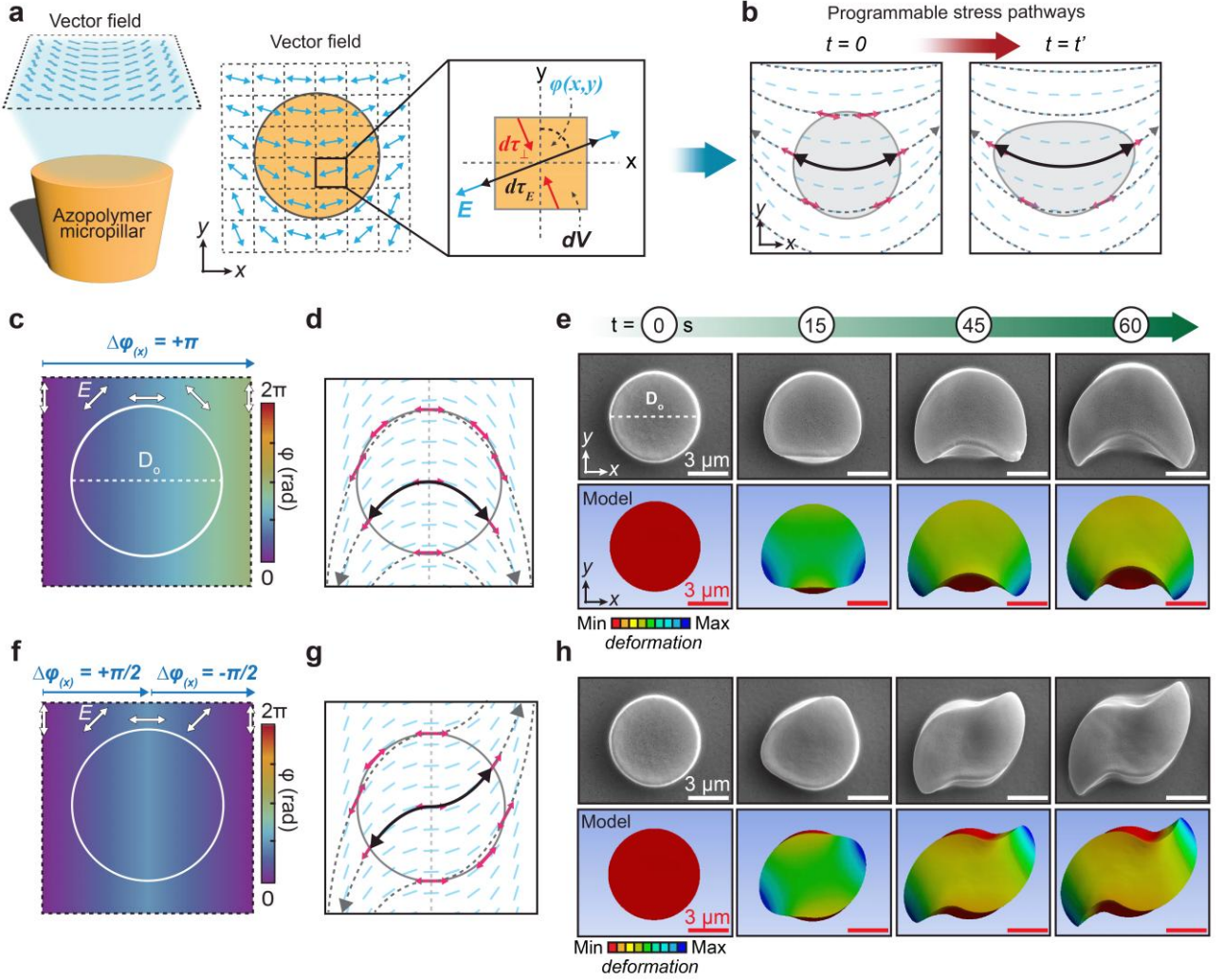


Fig 4. The vectorial field-guided deformation. **a)** Illustration of vector beam illumination on a micropillar and the building mechanism of local stress generated within the micropillar volume. **b)** Programmable stress pathways produced by the vector field in **a)** at initial and subsequent exposure times. **c)** Polarization map with $\Delta\phi_{(x)} = +\pi$ rotation of local linear polarization. **d)** Stress pathways scheme emerging from the illumination of the micropillar using the polarization map in **c)**. **e)** SEM (top row) and model (bottom row) images of the morphological evolution of the vectorial field-guided photo-deformation of the micropillar with inverted U-shape. **f)** Polarization map with $+\frac{\pi}{2}$ rotation in the first half of the square map and then with $-\frac{\pi}{2}$. **g)** Stress pathways scheme emerging from the illumination of the micropillar using the polarization map in **f)**. **h)** SEM (top row) and model (bottom row) images of the morphological evolution of the vectorial field-guided photo-deformation of the micropillar with S-shape. The modeled micropillar is designed to have $D_o = 6.7 \mu\text{m}$, matching with the experimental micropillar design. The colormap represents vertical displacement: red corresponds to the initial state, while dark blue indicates the maximum downward displacement.

According to this description, the polarization map in Fig. 4c was designed by gradually rotating the polarization azimuth ϕ clockwise from 0 to π along the x-axis of a square segment of $\sim 12 \times 12 \mu\text{m}^2$, while remaining uniform along the y-axis. In the figure, the circular profile of the pristine pillar and

its position relative to the designed polarization map is visualized as a white circle of diameter D_0 . Such a polarization field (see Fig. S11 for the optical characterization) induces an inverted U-shaped stress pathway inside the micropillar volume (Fig. 4d), which consistently guides the deformation of the azopolymer micropillar in the experiment (Fig. 4e, top row). The results of the VPA modeling quantitatively reproduce the observed morphology (Fig. 4e, bottom row) and its temporal dynamics (see also Movie S2). In addition, Fig. 4f shows another square polarization map where the azimuth angle φ is designed to rotate along the x-axis progressively by $\Delta\varphi = +\pi/2$ from the left edge to the center and then by $\Delta\varphi = -\pi/2$ from the center to the right edge. This design is apparently similar to the previous case, since it has the same initial and final polarization directions. However, it is characterized by a different relative spatial evolution of the azimuth angle, which generates a chiral stress pathway (Fig. 4g) that leads to the final experimental and modeled S-shaped microstructure shown in Fig. 4h (see also Movie S2).

The striking difference observed in the morphologies of the structures Fig. 4e and Fig. 4h demonstrates the critical role of the induced mechanical stress in the azomaterial photo-reconfiguration process, providing clear evidence of the validity of the VPA model in the general case of structured light irradiation. Not only the local polarization state, but also the spatial evolution dynamics of the polarization ultimately define the actual stress pathway. Structured vectorial light fields then become a powerful tool for guiding the morphological reconfiguration of the microstructures.

Importantly, the polarization maps are not limited to unidirectional uniform linear variations, but can have other spatial dependencies, such as angular evolutions and include discontinuities. Due to the circular profile of our particular pristine micropillars, a relevant example is the polarization maps designed with cylindrical symmetry in a polar coordinate system that uses the micropillar center as the origin of the reference system. In this case, the polarization direction φ in the x-y plane depends only on the polar angle θ , while it is uniform along the radial coordinate. Fig. 5a shows a first polarization map designed according to the functional dependence $\varphi(\theta) = \varphi_0 + \theta/2$, where $\varphi_0 = \pi/4$ is the polarization azimuth at $\theta = 0$. This polarization map is expected to generate stress pathways with triaxial symmetry (Fig. S10), whose geometry could also be visually represented in a simplified way by connecting the center of the pillar with the positions at the pillar perimeter where the local polarization is parallel to the local surface normal (the black solid arrows in Fig. 5b).

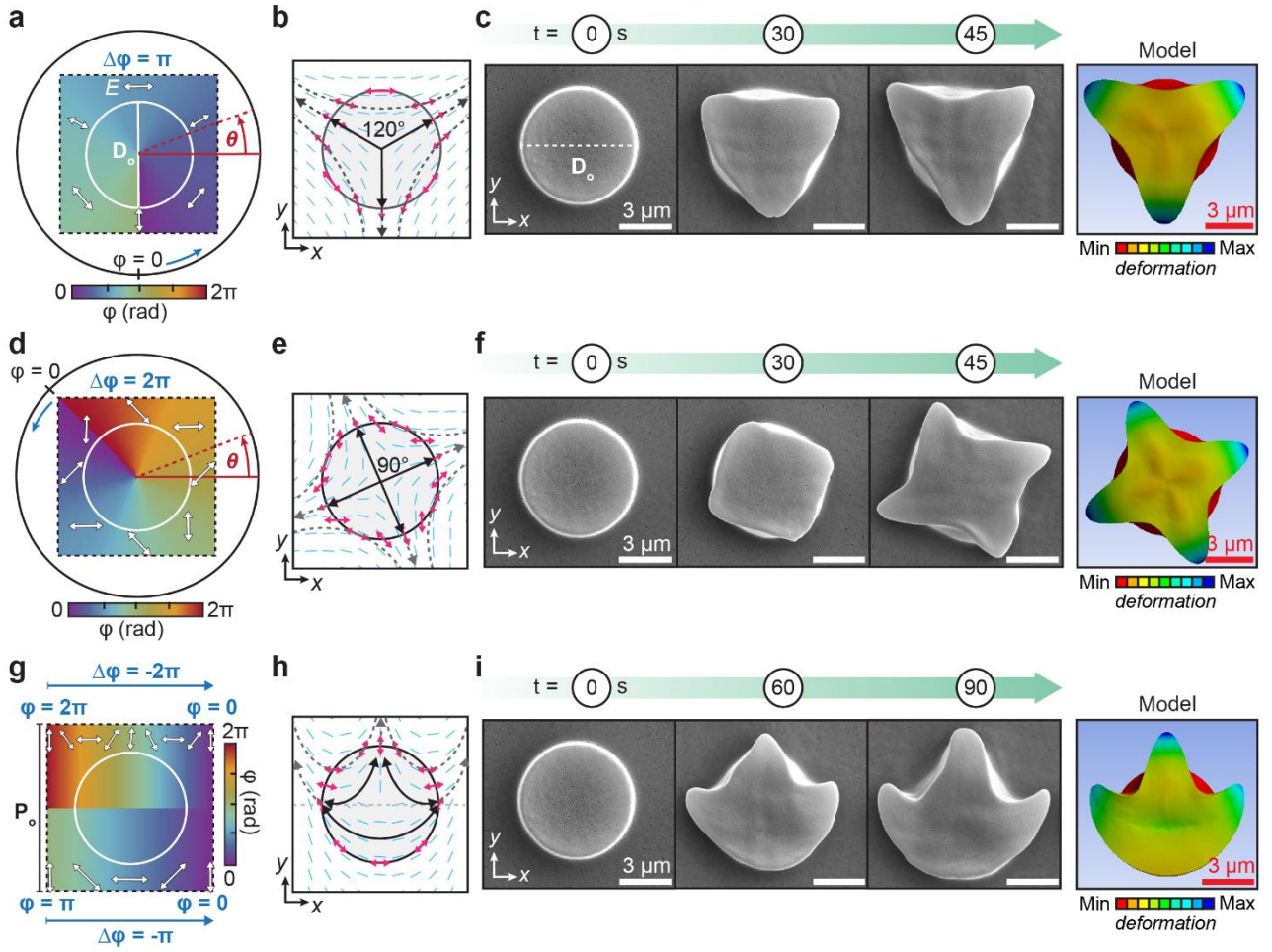


Fig 5. The diversity designs of the vectorial field-guided deformation. **a), d)** Polarization maps designed with rotation of azimuth angle following the equation $\varphi(\theta) = \varphi_0 + \theta/2$, and $\varphi(\theta) = \varphi_0 + \theta$ respectively. θ is polar coordinate θ , in the x-y plane, with the origin at the center of the micropillar. **b), e)** Stress pathways emerging from **a)** and **d)** polarization maps with triaxial and quadriaxial configurations, respectively. **c), f)** SEM images at different exposure times and model images using 45 seconds of exposure times, of the reconfigured micropillars exposed to the vectorial fields with polarization maps designed in **a)** and **d)**. **g)** Polarization map with tessellated approach. The top region designed to undergo -2π rotation, bottom region designed to undergo $-\pi$ rotation. **h)** Emerging stress pathways. **i)** SEM images at different exposure times and model images using 90 seconds of exposure times.

Photo-reconfiguration experiments and VPA modeling in Fig. 5c show the expected “tripetal” anisotropic microstructure resulting from irradiation with the designed structured polarization pattern. Notably, such a design is accompanied by a polarization singularity line in the optical field at $\theta = 3\pi/2$ (see also Fig. S11). However, its role in the photo-reconfiguration dynamics was negligible due to the size of the pristine micropillar, which was significantly larger than the region of zero field intensity within the singularity. It is worth mentioning that the polarization rotation in the ANSYS software is implemented as a local rotation of the element coordinate systems (see Materials and Methods) and does not take into account any polarization singularities. Then, the agreement of the

modeled reconfigured microstructure with the experimental one further confirmed the little influence of the optical singularity in this case. By adjusting the rotation angle of the local linear polarization, the number of stress pathways can be further increased (Fig. 5 d-f). The polarization map shown in Fig. 5d was designed as $\varphi(\theta) = \varphi_0 + \theta$, in which the local linear polarization undergoes a full 2π rotation along the polar angle θ and $\varphi_0 = 5\pi/4$. This design creates a quadriaxial system of stress pathways (Fig. 5e), resulting in a photo-reconfigured “quadrupetal” anisotropic microstructure in the model (see also Movie S3), as well as in the experiments (Fig. 5f).

Furthermore, Fig. 5g-i demonstrates the extension of the concept to multiaxial stress-pathways generated by composing multiple polarization maps. The map in Fig. 5g was designed by segmenting the target area into two rectangular tiles with linearly varying polarization patterns. The upper half of the map features a -2π rotation of linear polarization from the left to the right edge, while the lower half undergoes a linear $-\pi$ rotation. This polarization field generates three curved stress pathways as shown in Fig. 5h, which deform the microstructure into a peculiar “trident-shaped” anisotropic architecture, correctly described by the VPA model (Fig. 5i and Movie S3).

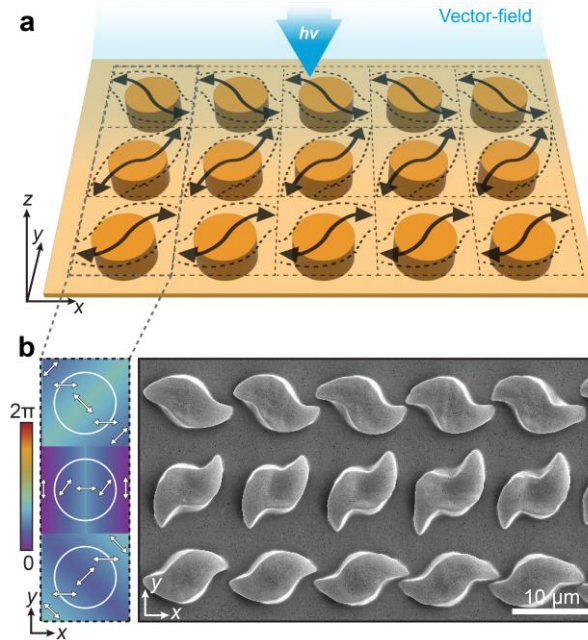


Fig 6. Programmable anisotropic designs in the array. **a)** Illumination scheme of a 5x3 azopolymer micropillar array, featuring spatially selective exposure and locally designed vector field. **b)** Polarization maps generated starting from the S-shapes architecture and by applying three different rotations of the azimuth angle φ (left); SEM image of the reconfigured 5x3 micropillar array. Each row of pillars was exposed to a distinct vector field.

As the last step, we demonstrate that the same stress-driven photo-reconfiguration mechanism driving single pillar deformation can be scaled to the entire array fitting into the optical field of view of the projection system (Fig. 6). Given that surface functionality typically arises from the formation of

structured arrays rather than from isolated elements, this approach unlocks the potential for creating large-area, multifunctional surface architectures.^{46,47}

Fig. 6a schematized a squared segmented vector field that is aligned with the array of micropillars. Here, the S-shaped geometry shown in Fig. 4f-h was chosen as the base architecture for local pillar reconfiguration in each segment. The segments were then globally rotated by three different angles with respect to the pillar centers, as visible in the polarization maps in Fig. 6b (left column). After exposure, the resulting surface morphologies in the SEM images show the expected array of complex S-shaped microarchitectures with varying global rotations, clearly demonstrating the ability of our vectorial light fields to tailor the shape of surface arrays into desired, on-demand architecture with complex anisotropy.

Discussion

In this study, we introduce the vectorial field-guided lithography as a new approach for the stress-driven photo-reconfiguration of azopolymer microstructures. By exploring the core concept of the recent Viscoplastic PhotoAlignment (VPA) model for the photo-deformation of azopolymers, we were able to completely describe the material reconfiguration process from the emergence of light-driven stress pathways, which directly reflect the vectorial and directional nature of polarized light. Using this approach, we have shown complex surface microstructures, having anisotropic, bent, and even chiral morphology. All of these microstructures have been achieved in one step of light irradiation with structured patterns of linear polarization, starting from a single pristine geometry of a pre-patterned azopolymer micropillars.

Importantly, we have demonstrated that the VPA model not only is valid in the case of homogeneous polarization patterns, but it holds in the general case of fully structured light. Furthermore, we have shown the predictive power of the model for the light-induced deformation dynamics of azopolymers. For the first time, a comprehensive theoretical framework shows quantitative predictive capabilities, even opening up to the inverse design approaches of the surface morphology, where the optical field producing a target morphology can be defined and optimized ahead of the experiment.

The core of our experimental optical system was the digital polarization rotator implemented through a conventional reflective SLM. This system allows to highlight the extreme flexibility of the vectorial photo-reconfiguration of azopolymer surfaces. Although the technical limits in terms of spatial and angular resolution associated with the polarization control through a conventional SLM, high-end devices, already commercially available could even boost the capabilities of our approach because of enhanced addressable phase levels (e.g. from 10-bit SLMs) and high-resolution displays (e.g. 4k pixel

resolution). This could potentially lead to the control of the vectorial photo-deformation of even submicron azopolymer microstructures.

Notably, the area of the sample simultaneously addressable by the vectorial photo-deformation in a single exposure step depends on the optical projection system (using a microscope objective in our case). However, stitching and tiling of the sample through motorized stage can easily scale up the structuring capabilities of the system to large areas, opening up to a new approach for fabrication of complex functional surfaces with on-demand anisotropies.

In conclusion, by harnessing structured vector fields, we have achieved programmable, stress-driven morphologies that move beyond traditional light intensity-driven approaches, marking a novel paradigm where the polarization, and not just light intensity alone, becomes a primary design parameter in optical lithography. Importantly, the same photo-deformation phenomenology can be achieved with any other light modulator capable of producing structured light, such as digital micromirror devices, and even optical metasurfaces. If the pre-patterned surface is prepared with higher resolution features (e.g. submicron), even the polarization singularities of the engineered structured field could play a role in the photo-reconfiguration, providing even additional control. This capability unlocks a wide range of potential applications across diverse fields, including unidirectional wettability control,³¹ directional structural adhesion,⁴⁸ surface-based information encoding,⁴⁹ and 3D microstructural-enhanced acoustic streaming.⁵⁰

Materials and Methods

Azopolymer synthesis and fabrication of the micropillar array

The azopolymer used in this study was synthesized by radical polymerization of the photosensitive monomer (E)-2-(4-((4-methoxyphenyl) diazenyl)phenoxy)ethyl acrylate, based on the previously reported procedure.³¹ Reagents were purchased from Merck and used without further purification. Details of optical absorbance (see also Fig. S1), thermal analysis, and molecular weight distribution have been reported in previous works.^{31,33}

The pre-structured film with micropillar array on the glass substrate was fabricated using a soft lithography technique as illustrated in Fig. S2. First, a polydimethylsiloxane (PDMS) soft stamp was fabricated by transferring the surface pattern from a silicone master.^{31,39} This process resulted in a PDMS stamp with a negative surface geometry with respect to the target pattern. A 10 wt% azopolymer solution in 1,1,2,2-tetrachloroethane was then deposited onto a standard glass microscope coverslip. The prepared PDMS stamp was then gently placed on the azopolymer solution, allowing

the azopolymer solution to infiltrate the negative pattern on the stamp. The sample was then left at room temperature for approximately 5 hours to allow the solvent in the azopolymer solution to completely evaporate. Finally, the PDMS stamp was carefully removed from the azopolymer surface, leaving the pre-structured azopolymer surface on the glass substrate to be used in the experiment. The azopolymer micropillars were designed from different silica masters, with height, H_o , diameter, D_o , and periodicity, P_o , varied according to the experiment being performed.

Micropillar deformation by homogeneous linearly polarized light

The experimental study of homogeneous linearly polarized light irradiation was performed using an expanded and collimated 488 nm laser (Coherent OBIS 488 LS) with the intensity at the surface plane set to about 160 mW/cm². The pristine micropillars had a measured height of $H_o \approx 8.4 \mu\text{m}$, diameter of $D_o \approx 4.0 \mu\text{m}$, and periodicity of $P_o 10.0 \approx \mu\text{m}$.

Digital polarization rotator

The optical setup as shown in Fig. 3b was based on a Coherent Sapphire 488 LP laser that emits a linearly polarized beam at a wavelength of 488 nm. The beam was expanded by two lenses, with focal length $f_1 = -50 \text{ mm}$ and $f_2 = 250 \text{ mm}$, respectively. This beam expansion increased the beam diameter to uniformly illuminate the entire active area of the Spatial Light Modulator (SLM). In addition, the lenses were arranged to achieve the desired beam waist and divergence for optimal projection. It is important to note that the lens configuration did not form a strictly afocal system (as the distances between lenses is $d_{21} = 380 \text{ mm}$) where the image was formed at infinity. Instead, the lenses were positioned to image the light pattern produced by the polarization rotator at a finite distance. This choice minimized the number of optical components in the setup with respect to a conventional $4f$ scheme, contributing to a more compact and efficient system. The polarization rotator unit consisted of a reflective SLM (Meadowlark Optics, Inc., phase-only, 1920 pixels by 1152 pixels), located between crossed quarter-waveplates (QWP I and QWP II). The fast axes of QWP I and II were oriented at $\pm 45^\circ$ respectively to input beam polarization direction. This combination comprises a variable phase-retarder, rotating the plane of polarization of a linearly polarized input beam by $d\theta$, where $d\theta$ is set by the programmable optical retardation as determined by the gray value addressed to the SLM. The quantitative characterization of the dependence of the output polarization direction on the input gray value addressed to the SLM was performed by positioning a linear polarizer immediately after QWP II. The results, as shown in Fig. S5, indicate a rotation of 1.4° per grayscale increment, demonstrating that 0 to 2π radians of rotation can be imparted by each SLM pixel over 0 to 255 grayscale values.

The spatially structured beam was then projected onto the sample plane by a 40X objective with 0.65 NA. The illuminated area corresponded to a demagnified image of the SLM screen with a projected area of approximately $130\ \mu\text{m} \times 78\ \mu\text{m}$. The beam had a total power of 0.7 mW. With this demagnification of the SLM screen, the distance between the pixels on the sample plane was approximately $0.07\ \mu\text{m}$ (with a density of ~ 15 pixels per μm), resulting in continuous diffraction-limited spatial modulation of the polarization azimuth.

Micropillar deformation through the digital polarization rotator

For collective pillar reshaping (Fig. 3) an array with measured geometrical parameters $H_o \approx 3.0\ \mu\text{m}$, $D_o \approx 4.0\ \mu\text{m}$, and $P_o \approx 10\ \mu\text{m}$ was used. The individual micropillar deformation experiment (Fig. 4 - 6) was performed by using an array of azopolymer micropillars with measured geometrical parameters $H_o \approx 3.0\ \mu\text{m}$, $D_o \approx 6.7\ \mu\text{m}$, and $P_o \approx 12\ \mu\text{m}$. To target each micropillar in the array with a $P_o \approx 10\ \mu\text{m}$, a box-shaped polarization map with area of $10 \times 10\ \mu\text{m}^2$ was used, which corresponds to 148×148 pixels in the grayscale image representing the target polarization map. In case of $P_o \approx 12\ \mu\text{m}$, a box-shaped polarization map with area of $12 \times 12\ \mu\text{m}^2$ was used corresponding to 178×178 pixels in the grayscale polarization design image.

To control the surface plane of the sample in all possible degrees of freedom, a sample holder was placed on an X-Y-Z stage integrated with gimbal mount. The alignment and the light focusing on a specific region of the azo micropillar array was performed by the motorized stages and the gimbals, using a bright field imaging system with a CCD camera as visual feedback.

Morphological characterization of microstructures

The morphological characterization of the surface was performed using Scanning Electron Microscopes (Hitachi SU5000, and FEI Nova NanoSEM 450). Prior to image acquisition, the sample underwent a process of metallic coating with a gold layer to increase the conductivity of the surface. The images were obtained using an acceleration voltage of 15 kilovolts and a high vacuum configuration, which is the standard setting for non-conductive samples with a thin conductive layer on the surface in this SEM. The magnifications used for imaging ranged from $1000\times$ to $9000\times$, depending on the scale of the object of interest.

Modeling of light-induced stress inside the azopolymer-based microvolume

Viscoplastic modeling of topographical structures was carried out using the finite element software ANSYS. Specifically, the Perzyna model was employed to describe the relationship between the rate of plastic strain $\dot{\varepsilon}_{pl}$ and the magnitude of light-induced stress τ_0 :

$$\dot{\epsilon}_{pl} = \gamma \left(\frac{\tau_0}{\tau_{yield}} - 1 \right) \quad (3)$$

Where τ_{yield} represents the yield stress and the parameter $\gamma = \tau_{yield}/(3\eta)$ defines the viscosity η of the plastic flow. The material properties of the amorphous azopolymer were characterized by the following parameters: $\tau_{yield} = 5$ MPa and $\gamma = 2.5 \times 10^{-3} \text{ s}^{-1}$. The initial tensile component $\tau_E = 2\tau_0/3$ was set to 25 MPa for Fig. 2f and 12.5 MPa for Fig. 4-5. Light absorption was explicitly considered in the model (with the assumed penetration depth of 5.2 μm for the light at 488 nm, selected according to the empirical comparison of three-dimensional morphology of the modeled structures and the analysis in our previous investigation³³). It is important to note that the simulation time for Fig. 2f was rescaled, where 1 second in the model corresponded approximately to 13 seconds in the experiment.

The model had a cylindrical shape with different boundary conditions. The bottom surface of the sample was ‘glued’ to the substrate, restricting both rotational and translational movement. In contrast, the upper and side surfaces were left free to deform. To address the computational challenges while maintaining accuracy, a combination of coarse and fine meshing strategies was employed. Critical regions of the cylindrical geometry, such as the top and bottom surfaces where light-induced deformation occurs, were refined using an element size of 0.25 μm , while less critical areas were discretized with a coarser mesh of 0.5 μm . The finite element mesh was generated using the ANSYS Meshing module, resulting in structured tetrahedral meshes composed of 6862 elements for Fig. 2 and 8733 elements for Figs. 4 and 5, suitable for subsequent finite element analysis.

The light-induced stress tensor was incorporated in ANSYS software using the custom subroutine Userthstrain.¹⁶ The thermal strain was chosen in this subroutine with the help of the Perzyna model (3) in such a way that it produced the plastic strain prescribed locally by the light-induced stress. To implement the polarization rotation, each model element was assigned a local coordinate system with the x-axis aligned along the direction of local linear polarization and the z-axis perpendicular to the substrate surface.

Author contributions

Conceptualization: S.L.O., D.McG. M.Sap.

Investigation: IK.J., M.Sal., F.R., N.L., P.P., D.McG., C.P., F.B.

Methodology: IK.J., D.McG., M.Sap., S.L.O.

Software: N.L., P.P.

Resources: S.L.O., F.B., M.Sal., D.McG.

Visualization: IK. J., F.R., M.Sal., N.L.

Supervision: S.L.O.

Writing original draft: IK.J. F.R., M.Sap., S.L.O.

Writing – review & editing: M.Sal., M.Sap., D.McG., S.L.O.

Data Availability

Source data are available for this paper. All other data that support the findings of this study are available from the corresponding authors upon reasonable request.

Acknowledgments

This work is supported by ERC grant (HyperMaSH, 101164874), funded by the European Union, Views and opinions expressed are however those of the authors only and do not necessarily reflect those of the European Union or the European Research Council Executive Agency. Neither the European Union nor the granting authority can be held responsible for them. M.Sap., N.L., and P.P acknowledge support from the grant GR 3725/10-1 from Deutsche Forschungsgemeinschaft. D.McG. and C.P. acknowledge support from US National Science Foundation (NSF) Division of Electrical, Communications and Cyber Systems, award number 2024118, and NSF Division of Materials Research, award number 1919557.

Conflict of interest

The authors declare no conflicts of interest.

Supplementary Information

Supplementary information accompanies the manuscript on the Light: Science & Applications website (<http://www.nature.com/lisa>).

References

1. Johnson, M. R. W. & Harley, S. L. *Orogenesis: The Making of Mountains*. (Cambridge University Press, 2012).
2. Tallinen, T. *et al.* On the growth and form of cortical convolutions. *Nature Phys* **12**, 588–593 (2016).
3. Yang, S. *et al.* Morphogens enable interacting supracellular phases that generate organ architecture. *Science* **382**, eadg5579 (2023).

4. Guo, K., Huang, C., Miao, Y., Cosgrove, D. J. & Hsia, K. J. Leaf morphogenesis: The multifaceted roles of mechanics. *Molecular Plant* **15**, 1098–1119 (2022).
5. Wittmann, R., Nguyen, G. H. P., Löwen, H., Schwarzendahl, F. J. & Sengupta, A. Collective mechano-response dynamically tunes cell-size distributions in growing bacterial colonies. *Commun Phys* **6**, 331 (2023).
6. Bae, H. J. *et al.* Self-organization of maze-like structures via guided wrinkling. *Sci. Adv.* **3**, e1700071 (2017).
7. Chen, S., Chen, J., Zhang, X., Li, Z.-Y. & Li, J. Kirigami/origami: unfolding the new regime of advanced 3D microfabrication/nanofabrication with “folding”. *Light Sci Appl* **9**, 75 (2020).
8. Wang, B., Bao, S., Vinnikova, S., Ghanta, P. & Wang, S. Buckling analysis in stretchable electronics. *npj Flex Electron* **1**, 5 (2017).
9. Liu, N. *et al.* Wrinkled Interfaces: Taking Advantage of Anisotropic Wrinkling to Periodically Pattern Polymer Surfaces. *Advanced Science* **10**, 2207210 (2023).
10. Liu, N. *et al.* Smart Wrinkled Interfaces: Patterning, Morphing, and Coding of Polymer Surfaces by Dynamic Anisotropic Wrinkling. *Langmuir* **40**, 18837–18856 (2024).
11. Jia, Q. *et al.* Optical manipulation: from fluid to solid domains. *Photonics Insights* **2**, R05 (2023).
12. Yan, S. *et al.* Photo-induced stress relaxation in reconfigurable disulfide-crosslinked supramolecular films visualized by dynamic wrinkling. *Nat Commun* **13**, 7434 (2022).
13. Oscurato, S. L., Salvatore, M., Maddalena, P. & Ambrosio, A. From nanoscopic to macroscopic photo-driven motion in azobenzene-containing materials. *Nanophotonics* **7**, 1387–1422 (2018).
14. Saphiannikova, M., Toshchevikov, V. & Tverdokhle, N. Optical deformations of azobenzene polymers: orientation approach vs. other concepts. *Soft Matter* **20**, 2688–2710 (2024).

15. Yadavalli, N. S., Saphiannikova, M. & Santer, S. Photosensitive response of azobenzene containing films towards pure intensity or polarization interference patterns. *Applied Physics Letters* **105**, 051601 (2014).
16. Loebner, S. *et al.* Local Direction of Optomechanical Stress in Azobenzene Containing Polymers During Surface Relief Grating Formation. *Macro Materials & Eng* **307**, 2100990 (2022).
17. Yadav, B., Domurath, J., Kim, K., Lee, S. & Saphiannikova, M. Orientation Approach to Directional Photodeformations in Glassy Side-Chain Azopolymers. *J. Phys. Chem. B* **123**, 3337–3347 (2019).
18. Borbone, F. *et al.* Enhanced photoinduced mass migration in supramolecular azopolymers by H-bond driven positional constraint. *J. Mater. Chem. C* **9**, 11368–11375 (2021).
19. Strobelt, J., Van Soelen, M., Abourahma, H. & McGee, D. J. Supramolecular Azopolymers for Dynamic Surface Microstructures Using Digital Polarization Optics. *Advanced Optical Materials* **11**, 2202245 (2023).
20. Loebner, S. *et al.* Light-Induced Deformation of Azobenzene-Containing Colloidal Spheres: Calculation and Measurement of Opto-Mechanical Stresses. *J. Phys. Chem. B* **122**, 2001–2009 (2018).
21. Oscurato, S. L. *et al.* Shapeshifting Diffractive Optical Devices. *Laser & Photonics Reviews* **16**, 2100514 (2022).
22. Reda, F., Salvatore, M., Astarita, M., Borbone, F. & Oscurato, S. L. Reprogrammable Holograms from Maskless Surface Photomorphing. *Advanced Optical Materials* **11**, 2300823 (2023).
23. Oscurato, S. L. *et al.* Large-Scale Multiplexed Azopolymer Gratings with Engineered Diffraction Behavior. *Adv. Mater. Interfaces* **8**, 2101375 (2021).

24. Reda, F., Salvatore, M., Borbone, F., Maddalena, P. & Oscurato, S. L. Accurate Morphology-Related Diffraction Behavior of Light-Induced Surface Relief Gratings on Azopolymers. *ACS Materials Lett.* **4**, 953–959 (2022).
25. Senel, O. *et al.* Continuous laser printing of surface relief gratings on azopolymer films. *Opt. Express* **32**, 47385 (2024).
26. Rekola, H., Berdin, A., Fedele, C., Virkki, M. & Priimagi, A. Digital holographic microscopy for real-time observation of surface-relief grating formation on azobenzene-containing films. *Sci Rep* **10**, 19642 (2020).
27. Strobelt, J., Van Soelen, M. & McGee, D. J. Direct laser writing of micrograting arrays using a spatial light modulator. in *Advanced Fabrication Technologies for Micro/Nano Optics and Photonics XVI* (eds. Von Freymann, G., Blasco, E. & Chanda, D.) 7 (SPIE, San Francisco, United States, 2023). doi:10.1117/12.2647393.
28. Audia, B., Tone, C. M., Pagliusi, P., Mazzulla, A. & Cipparrone, G. Hierarchical Fourier Surfaces via Broadband Laser Vectorial Interferometry. *ACS Photonics* **10**, 3060–3069 (2023).
29. Wang, Z., Hsu, C. & Wang, X. Topographical transition of submicron pillar array of azo molecular glass induced by circularly polarized light. *Sci Rep* **11**, 7327 (2021).
30. Hsu, C., Xu, Z. & Wang, X. Symmetry-Breaking Response of Azo Molecular Glass Microspheres to Interfering Circularly Polarized Light: From Shape Manipulation to 3D Patterning. *Adv Funct Materials* **29**, 1806703 (2019).
31. Oscurato, S. L., Borbone, F., Maddalena, P. & Ambrosio, A. Light-Driven Wettability Tailoring of Azopolymer Surfaces with Reconfigured Three-Dimensional Posts. *ACS Appl. Mater. Interfaces* **9**, 30133–30142 (2017).
32. Jo, W. *et al.* Light-Designed Shark Skin-Mimetic Surfaces. *Nano Lett.* **21**, 5500–5507 (2021).

33. Januariyasa, I. K., Borbone, F., Salvatore, M. & Oscurato, S. L. Wavelength-Dependent Shaping of Azopolymer Micropillars for Three-Dimensional Structure Control. *ACS Appl. Mater. Interfaces* **15**, 43183–43192 (2023).
34. Huang, H., Su, Y., Xu, J. & Wang, X. Asymmetric Morphology Transformation of Azo Molecular Glass Microspheres Induced by Polarized Light. *Langmuir* **35**, 15295–15305 (2019).
35. Lee, S., Kang, H. S., Ambrosio, A., Park, J.-K. & Marrucci, L. Directional Superficial Photofluidization for Deterministic Shaping of Complex 3D Architectures. *ACS Appl. Mater. Interfaces* **7**, 8209–8217 (2015).
36. Davis, J. A., McNamara, D. E., Cottrell, D. M. & Sonehara, T. Two-dimensional polarization encoding with a phase-only liquid-crystal spatial light modulator. *Appl. Opt.* **39**, 1549 (2000).
37. De Sio, L. D. *et al.* Digital polarization holography advancing geometrical phase optics. *Opt. Express, OE* **24**, 18297–18306 (2016).
38. Pirani, F. *et al.* Light-Driven Reversible Shaping of Individual Azopolymeric Micro-Pillars. *Sci Rep* **6**, 31702 (2016).
39. Salvatore, M., Borbone, F., Reda, F., Maddalena, P. & Oscurato, S. L. Programmable surface anisotropy from polarization-driven azopolymer reconfiguration. *J. Phys. Photonics* **3**, 034013 (2021).
40. Januariyasa, I. K., Reda, F., Borbone, F., Salvatore, M. & Oscurato, S. L. Molding three-dimensional azopolymer microstructures with holographically structured light. *RSC Appl. Interfaces* 10.1039.D4LF00092G (2024) doi:10.1039/D4LF00092G.

41. Toshchevikov, V., Ilnytskyi, J. & Saphiannikova, M. Photoisomerization Kinetics and Mechanical Stress in Azobenzene-Containing Materials. *J. Phys. Chem. Lett.* **8**, 1094–1098 (2017).
42. Holzapfel, G. A. *Nonlinear Solid Mechanics*. (John Wiley & Sons Ltd, Hoboken, NJ, USA, 2010).
43. Toshchevikov, V. & Saphiannikova, M. Photo-Ordering and Deformation in Azobenzene-Containing Polymer Networks under Irradiation with Elliptically Polarized Light. *Processes* **11**, 129 (2023).
44. Tverdokhlebov, N., Audia, B., Pagliusi, P. & Saphiannikova, M. Viscoplastic photoalignment modeling of asymmetric surface restructuring in azopolymer films by elliptically polarized light. *J. Mater. Chem. C* **13**, 1263–1271 (2025).
45. Gbur, G. J. *Singular Optics*. (CRC Press, Boca Raton, 2016). doi:10.1201/9781315374260.
46. Wang, Y. *et al.* Nature-inspired micropatterns. *Nat Rev Methods Primers* **3**, 68 (2023).
47. Ding, H. *et al.* Controlled Microstructural Architectures Based on Smart Fabrication Strategies. *Adv Funct Materials* **30**, 1901760 (2020).
48. Kwak, M. K., Jeong, H. E., Bae, W. G., Jung, H. & Suh, K. Y. Anisotropic Adhesion Properties of Triangular-Tip-Shaped Micropillars. *Small* **7**, 2296–2300 (2011).
49. Wu, L. *et al.* Printing Patterned Fine 3D Structures by Manipulating the Three Phase Contact Line. *Advanced Functional Materials* **25**, 2237–2242 (2015).
50. Harley, W. S., Kolesnik, K., Heath, D. E. & Collins, D. J. Enhanced acoustic streaming effects via sharp-edged 3D microstructures. *Lab Chip* 10.1039.D3LC00742A (2024) doi:10.1039/D3LC00742A.

Supplementary information for

Stress-driven photo-reconfiguration of surface microstructures with vectorial light fields

I Komang Januariyasa,¹ Francesco Reda,¹ Nikolai Liubimtsev,² Pawan Patel,^{2,3} Cody Pedersen,⁴ Fabio Borbone,⁵ Marcella Salvatore,¹ Marina Saphiannikova,^{2,3} David McGee,⁴ and Stefano Luigi Oscurato^{1,*}

¹Physics Department “E. Pancini”, University of Naples Federico II, Complesso Universitario di Monte Sant’Angelo, via Cinthia, 80126, Naples, Italy.

²Division Theory of Polymers, Leibniz Institute of Polymer Research Dresden, 01069 Dresden, Germany.

³Faculty of Mechanical Science and Engineering, Dresden University of Technology, 01062 Dresden, Germany

⁴ Department of Physics, The College of New Jersey, Ewing, New Jersey 08628, USA.

⁵Department of Chemical Sciences, University of Naples “Federico II”, Complesso Universitario di Monte Sant’Angelo, Via Cintia, 80126 Naples, Italy.

*Stefano Luigi Oscurato, e-mail: stefanolugi.oscurato@unina.it

*Marina Saphiannikova, e-mail: grenzer@ipfdd.de

*David J. McGee, e-mail: mcgeed@tcnj.edu

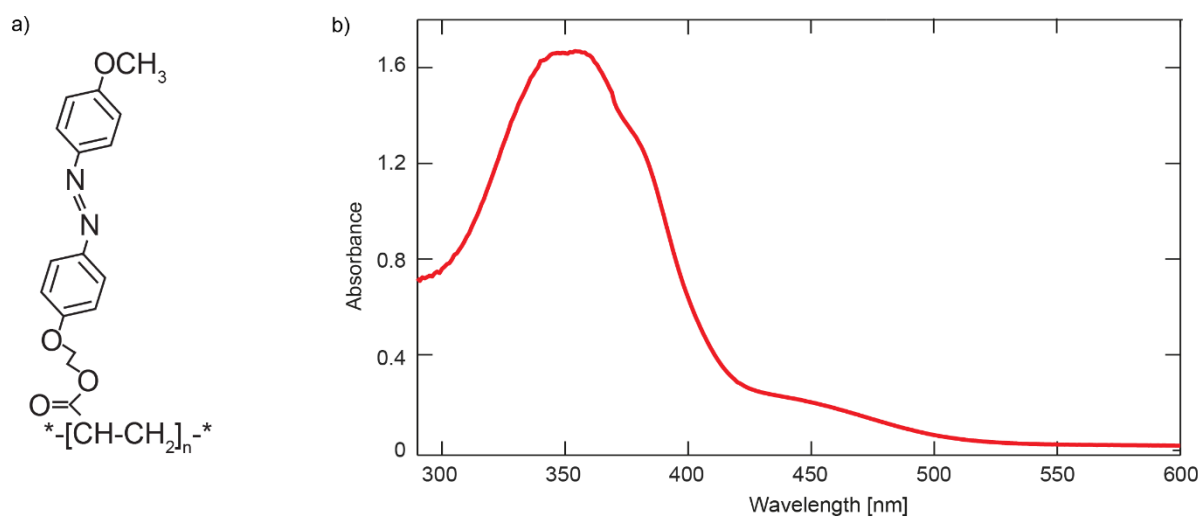


Figure S1. a) The chemical structure and b) the UV-Visible absorption spectrum of the azopolymer used in this study. The UV-Visible absorbance spectrum of the azopolymer was recorded with Jasco V560 spectrophotometer.

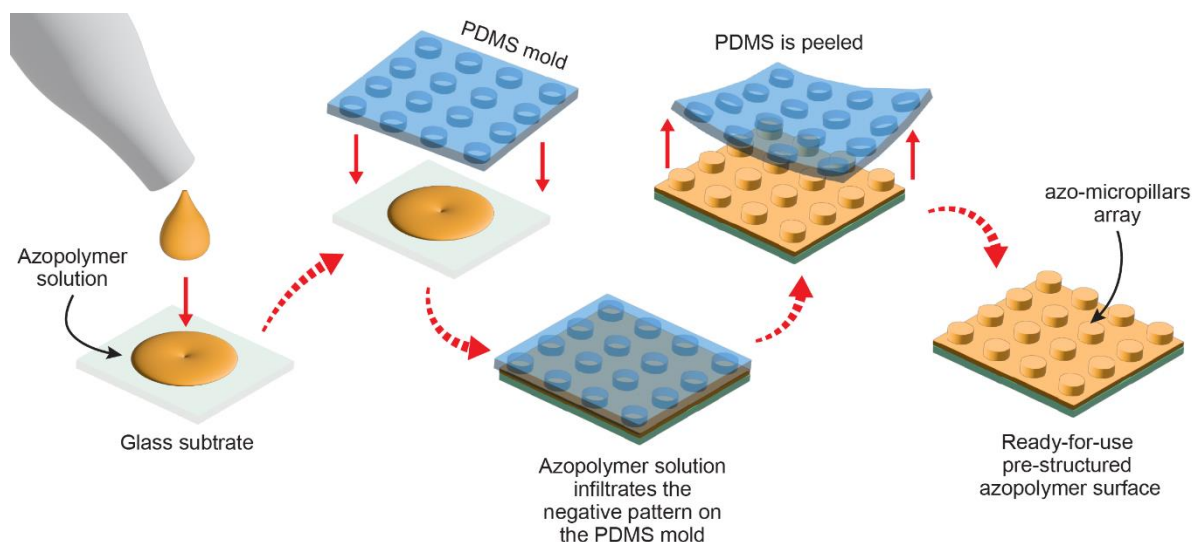


Figure S2. The procedure of the soft-lithography used to fabricate azo-micropillars array on the surface. A few drops of 10 wt% azopolymer solution in 1,1,2,2-tetrachloroethane was deposited onto a standard glass microscope coverslip. Then, the prepared PDMS stamp was gently placed onto the azopolymer solution, allowing the azopolymer solution to infiltrate the negative pattern on the stamp. The sample is then left at ambient temperature for approximately 5 hours, during which the solvent in the azopolymer solution evaporates completely. The final step is to carefully peel the PDMS stamp from the azopolymer surface, leaving the pre-structured azopolymer surface on the glass substrate to be used in the experiment. The pre-structured azo-micropillars can be selected to have a height (H_o), diameter (D_o), and periodicity (P_o) which are varied depending on the conducted experiment.

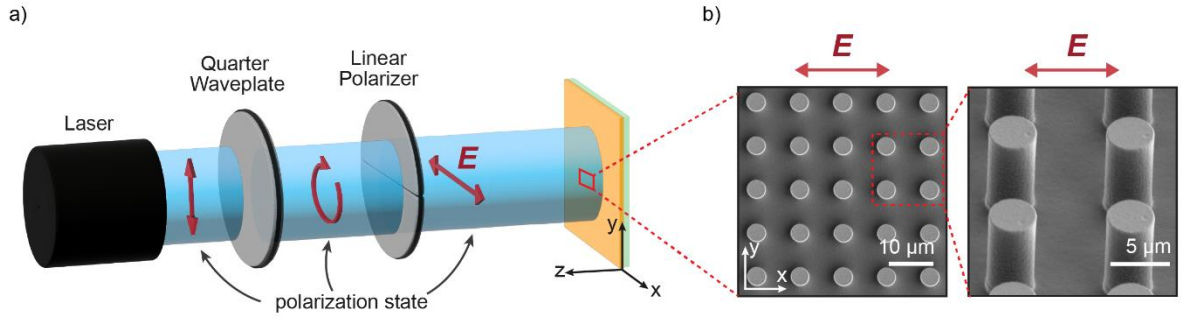


Figure S3. The illumination study of homogeneous beam with linear polarization. a) The optical configuration of the illumination exposure. The experimental study of homogeneous linearly polarized light irradiation was performed using a 488 nm laser (Coherent OBIS 488 LS) with the intensity on the surface plane set to about 160 mW/cm^2 . b) The morphology of the pristine state of the azo-micropillar observed from top-down and inclined view. The measured pristine azo-micropillars have a height of $H_o \approx 8.4 \text{ }\mu\text{m}$, diameter of $D_o \approx 4 \text{ }\mu\text{m}$, and periodicity of $P_o \approx 10 \text{ }\mu\text{m}$.

Supplementary note 1: Viscoplastic PhotoAlignment (VPA) modeling

1. Light-induced stress and orientation of backbone segments

The light induced stress $\boldsymbol{\tau}$ in the VPA modeling is defined by the rate of change of the 2nd order orientation tensor $\langle \mathbf{uu} \rangle$ of rigid segments of the polymer backbone:¹

$$\boldsymbol{\tau} = 3nkT\lambda_R \frac{\partial}{\partial t} \langle \mathbf{uu} \rangle. \quad (\text{S1})$$

Here \mathbf{u} is the unit orientation vector of the segment, n is the number density of segments and λ_R is their rotational time in the absence of light. The orientation state of rigid backbone segments is described by the 2nd and 4th order orientation tensors $\langle \mathbf{uu} \rangle$ and $\langle \mathbf{uuuu} \rangle$. The time evolution of 2nd order tensor can be calculated as follows:

$$\frac{\partial}{\partial t} \langle \mathbf{uu} \rangle = -\frac{5V_r}{6\lambda_R} \left\{ \hat{\mathbf{E}}\hat{\mathbf{E}} \cdot \langle \mathbf{uu} \rangle + \langle \mathbf{uu} \rangle \cdot \hat{\mathbf{E}}\hat{\mathbf{E}} - 2\hat{\mathbf{E}}\hat{\mathbf{E}} : \langle \mathbf{uuuu} \rangle \right\} - \frac{\langle \mathbf{uu} \rangle}{\lambda_R} + \frac{\boldsymbol{\delta}}{3\lambda_R}, \quad (\text{S2})$$

where $\hat{\mathbf{E}}$ is the unit vector of light polarization and $\boldsymbol{\delta}$ is the unit tensor. The parameter

$$V_r = 2qmV_0 / 5kT \quad (\text{S3})$$

is the reduced strength of orientation potential U_{eff} acting on the backbone segments irradiated with linearly polarized light:

$$U_{\text{eff}} = qmV_0 (\hat{\mathbf{E}} \cdot \mathbf{u})^2. \quad (\text{S4})$$

Here V_0 is the strength of orientation potential, which effectively describes the gradual orientation of azobenzene chromophores after several photoisomerization cycles. A derivation of effective orientation potential from kinetic equations for the photoisomerization dynamics between trans and cis-isomers of azobenzenes can be found in Ref. 2. Furthermore, it is assumed that each of the backbone segments contains m azobenzenes, whose orientation distribution with respect to the long axes of the segments is described by the shape factor q . For side chain azopolymers q is close to -0.5,³ which means that reorientation of azos perpendicular to the light polarization is transferred to an alignment of the polymer backbones along the same polarization direction. Note that the reduced strength V_r takes negative values because $q < 0$.

2. Homogeneous irradiation with linearly polarized light

The side-chain azopolymers align and stretch along the light polarization direction. Let's choose this direction as the axis x of local coordinate system (LCS). Under homogeneous irradiation, i.e. at the constant light intensity, the time evolution of the xx -component of the 2nd order orientation tensor is given by:

$$\frac{\partial}{\partial t} \langle u_x^2 \rangle = \frac{1}{\lambda_R} \left[V_r \left(\langle u_x^2 \rangle - 1 \right) \langle u_x^2 \rangle - \langle u_x^2 \rangle + \frac{1}{3} \right] \quad (S5)$$

This expression was derived in Supporting Information to Ref. 4. Due to the axial symmetry with respect to the light polarization, two other diagonal components are equal to each other:

$$\langle u_y^2 \rangle = \langle u_z^2 \rangle = (1 - \langle u_x^2 \rangle) / 2 \quad (S6)$$

and all off-diagonal components are equal to zero. Together with equation (S1), this means that the light induced stress τ is also diagonal and symmetric around the axis x in LCS:

$$\tau_{yy} = \tau_{zz} = -\tau_{xx} / 2. \quad (S7)$$

Hence, the tensile component of stress tensor $\tau_E = \tau_{xx}$ and the compressive components $\tau_{\perp} = -\tau_E / 2$. The time-dependent magnitude of τ_E is calculated from equation (S1) using equations (S5) and (S6) with the initial value of $\langle u_x^2 \rangle = 1/3$ which corresponds to isotropic orientation of backbone segments. The rotational time of polymer backbone segments is chosen to be long enough ($\lambda_R = 1000$ s) to achieve non-vanishing stress values in the VPA modeling of azopolymer micropillars. The reduced potential strength V_r in equation (S5) is prescribed by the magnitude of light induced tensile stress at the beginning of irradiation:⁴

$$\tau_E(0) = -\frac{2}{3} nkTV_r. \quad (S8)$$

By implementing the light induced stress tensor into the custom subroutine Userthstrain of the finite element software ANSYS, we are able to reproduce the uniaxial deformation of a homogeneously irradiated azopolymer micropillar. For that we apply the visco-plastic Perzyna model, described by equation (3) in the main text. More details about the implementation of light induced stress can be found in the PhD thesis of B. Yadav.⁵

3. Light induced stress at the initial stages of irradiation

The light induced stress in the VPA model is described by rather complicated tensorial equations (S1) and (S2), which contain the dyadic tensor $\hat{\mathbf{E}}\hat{\mathbf{E}}$ and the orientation tensors $\langle \mathbf{uu} \rangle$ and $\langle \mathbf{uuuu} \rangle$. This makes difficult for a non-theorist to comprehend a relation between the light induced stress and the light polarization. Fortunately, it is possible to find an elegant solution to this system of tensor equations, assuming that the initially isotropic state of polymer backbones changes very slowly under light irradiation. Under this condition, the light induced stress remains close to its value at the beginning of irradiation.

First, we immediately see that the last two terms in equation (S2) cancel each other out, since the initially isotropic state is described by $\langle \mathbf{uu} \rangle = \delta/3$. To simplify the expression in parentheses, it is necessary to apply a closure approximation to the 4th order orientation tensor $\langle \mathbf{uuuu} \rangle$. It is known that linear closure provides an exact solution for the random orientation of rods:⁶

$$\langle \mathbf{uuuu} \rangle = -\frac{1}{35} \Sigma_4 + \frac{1}{7} \langle \mathbf{uu} \rangle \cdot \Sigma_4 + \frac{1}{7} \Sigma_4 \cdot \langle \mathbf{uu} \rangle \quad (\text{S9})$$

where $\Sigma_4 = \delta\delta + \mathbf{I} + \mathbf{I}^+$ represents the sum of 4th order isotropic tensors. Applying the linear closure to the expression in parentheses of equation (S2) results in

$$\hat{\mathbf{E}}\hat{\mathbf{E}} \cdot \langle \mathbf{uu} \rangle + \langle \mathbf{uu} \rangle \cdot \hat{\mathbf{E}}\hat{\mathbf{E}} - 2\hat{\mathbf{E}}\hat{\mathbf{E}} : \langle \mathbf{uuuu} \rangle = \frac{2}{5} \hat{\mathbf{E}}\hat{\mathbf{E}} - \frac{2}{15} \text{Tr}(\hat{\mathbf{E}}\hat{\mathbf{E}}) \delta \quad (\text{S10})$$

While the trace of $\hat{\mathbf{E}}\hat{\mathbf{E}}$ is equal to 1 for any polarization state,

$$\frac{\partial}{\partial t} \langle \mathbf{uu} \rangle = -\frac{V_r}{3\lambda_R} (\hat{\mathbf{E}}\hat{\mathbf{E}} - \delta/3). \quad (\text{S11})$$

After substituting the time derivative of $\langle \mathbf{uu} \rangle$ into equation (S1),

we arrive to the equation (1) of the main text:

$$\boldsymbol{\tau} = \tau_0 (\hat{\mathbf{E}}\hat{\mathbf{E}} - \delta/3)$$

where $\tau_0 = -nkTV_r$ is the magnitude of light induced stress at the beginning of irradiation.

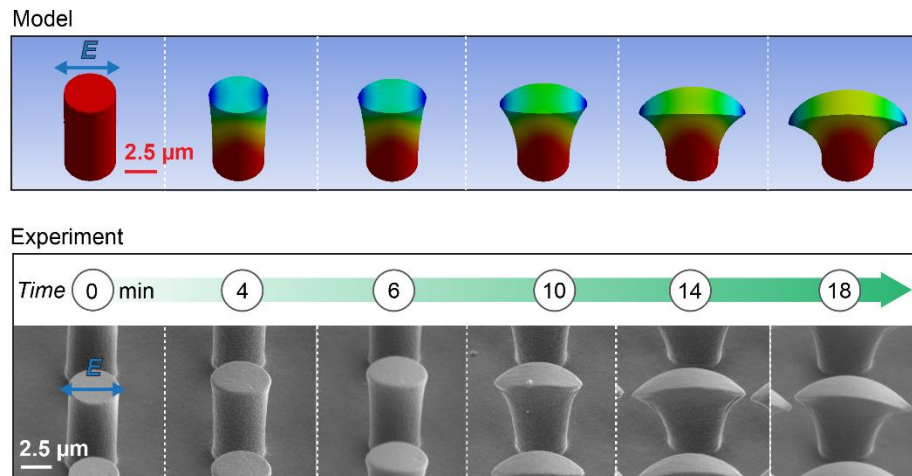


Figure S4. The basic study of the azo-micropillar deformation from a homogeneous linearly polarized beam. The morphological evolution of azo-micropillar from the model simulation (top row) and the experiment (bottom row) at different time points (0 – 18 min).

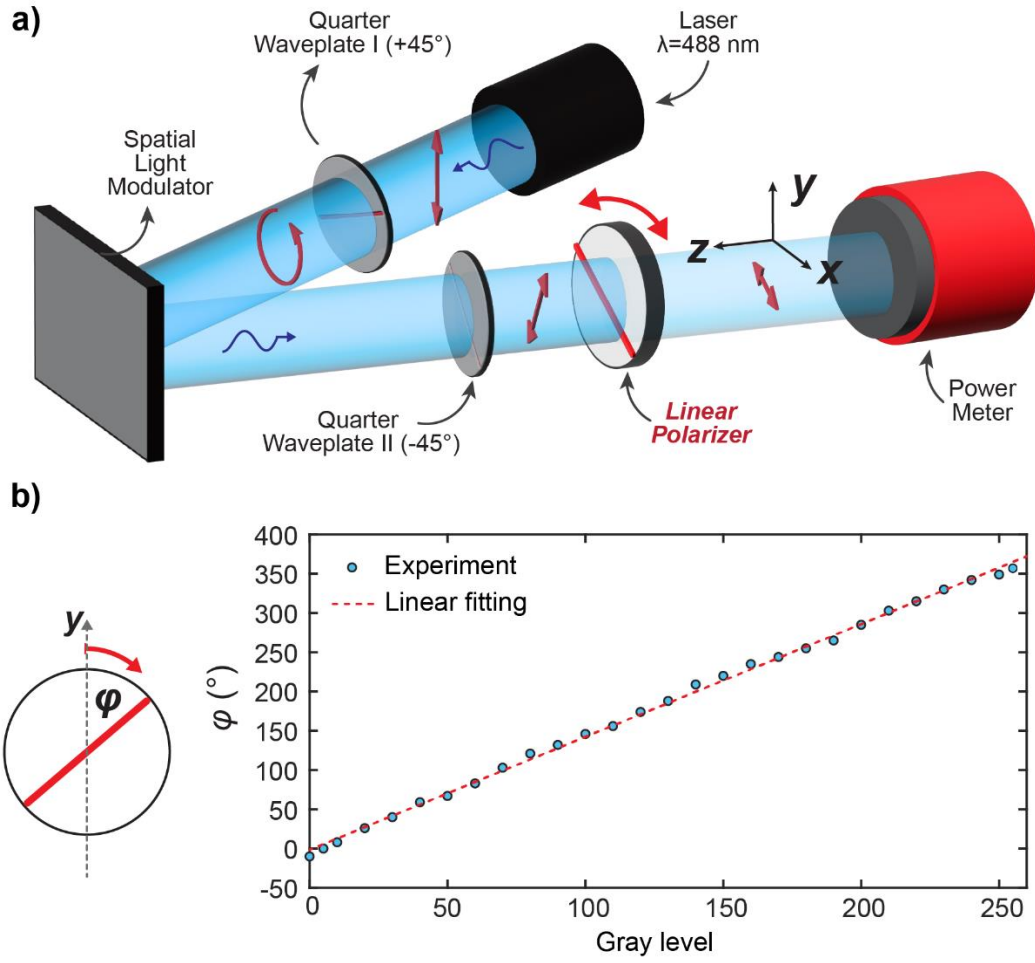


Figure S5. a) The optical setup for characterizing the digital polarization rotator. A characterization procedure was conducted to establish a conversion between the grayscale value in the image and the relative rotation of the polarization angle relative to a designated reference axis (the y -axis in this study). The procedure of this experiment is to input an image of uniform grayscale level (8-bit, $1920 \text{ pixels} \times 1152 \text{ pixels}$) into the spatial light modulator (SLM), which covered the entire active area, and then to measure the angle of the polarization axis (φ ; relative to the optical y -axis) when the power meter measured the maximum power output. This angle represented the major axis of polarization relative to the y -axis. The process is repeated for the entire range of grayscale values (i.e., from 0 to 255). b) The curve of conversion grayscale to polarization rotation and its linear fitting.

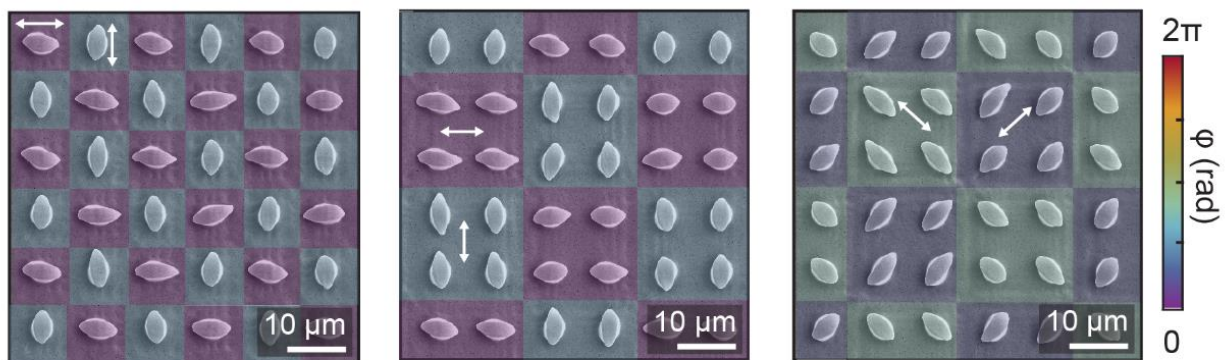


Figure S6. Surface reconfigurations with various checkerboard-styled polarization map designs, e.g., vertical-horizontal and diagonal with different numbers of micropillars for each polarization box.

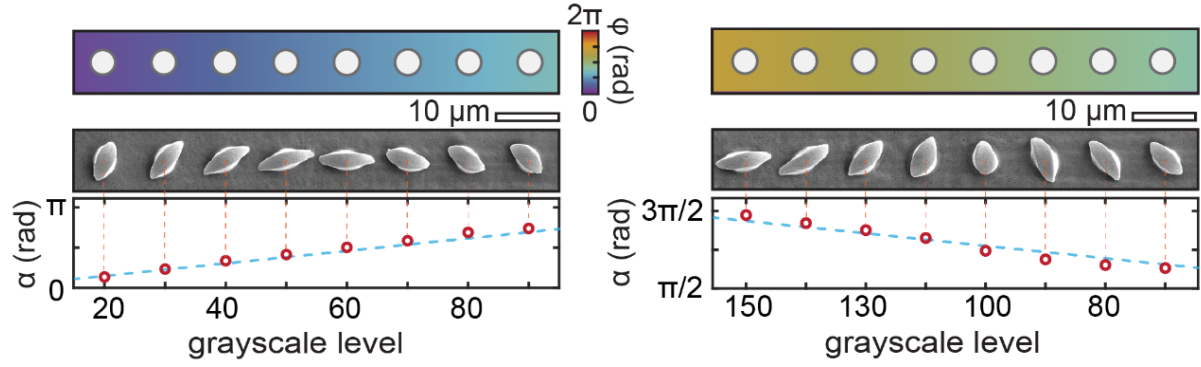


Figure S7. Surface reconfigurations with a gradual rotation of polarization azimuth across a row of micropillars. Each reconfiguration was produced with a random grayscale range (e.g., gradually increasing and decreasing trend in left and right data, respectively). α is the angle between the major axis of the micropillar elongation relative to y -axis in clockwise rotation. The correlation between the linearly varying polarization pattern and the resulting deformation orientation of the exposed micropillars was studied by measuring the deformation angles α as a function of the linearly increasing gray value assigned to the SLM. The analysis, shown in plot of gray level vs. α , shows that we achieved an excellent agreement with the expected picture of the gradually rotating stress pathways deforming the surface microstructures along the local polarization direction.

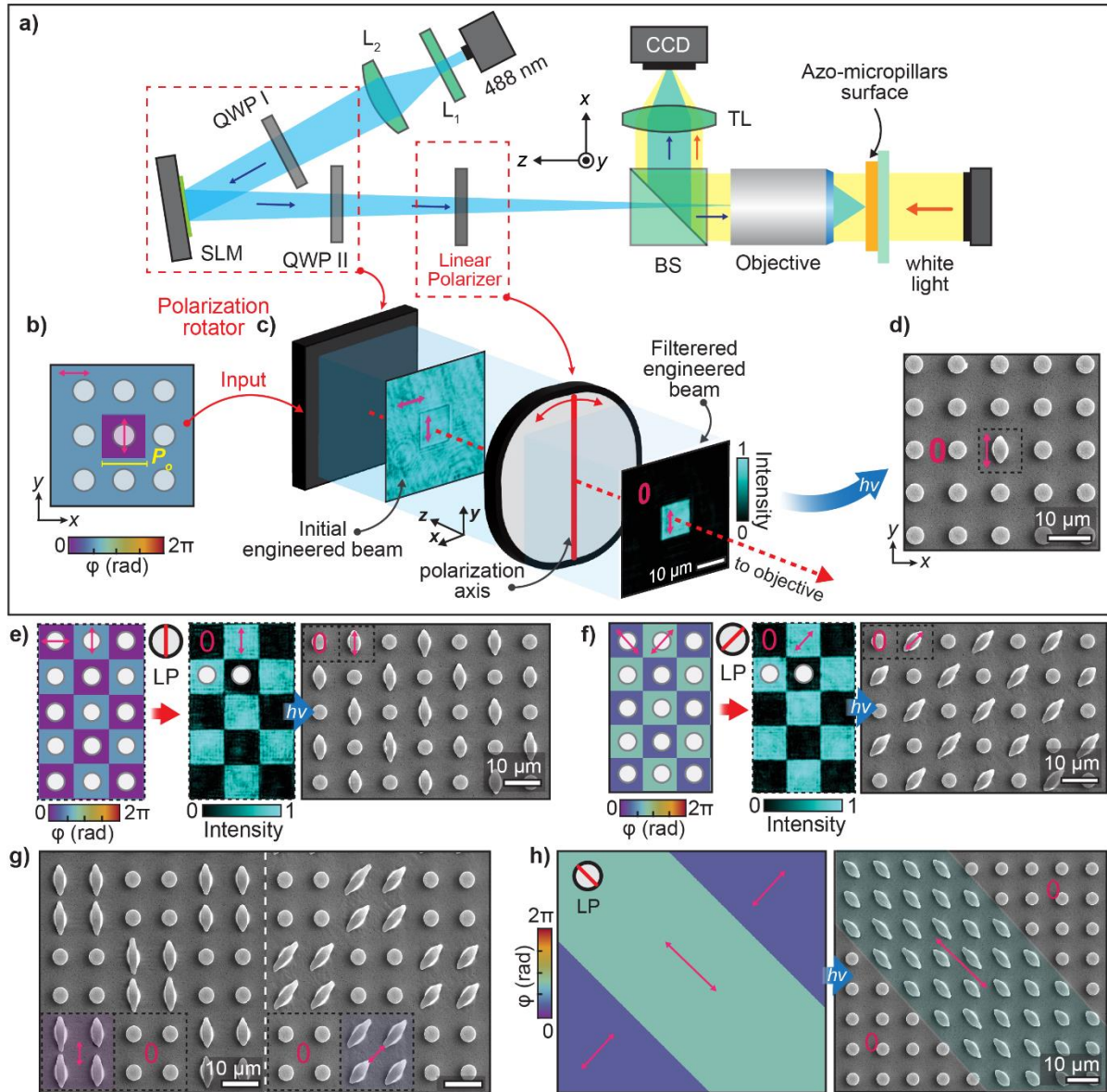


Figure S8. The introduction of the “polarization filter” strategy to impart a simple intensity-polarization control in the beam for complex surface configuration. **a)** The optical configuration of polarization rotator used in this study with an additional linear polarization after the polarization rotator part (i.e., after QWP II). **b)** The polarization map comprising a rectangular region exhibiting polarization rotation in the vertical direction ($\varphi = 0$), designed to occupy an area encasing a single micropillar ($P_o \times P_o$). The remaining portion of the polarization map is set to possess a polarization rotation in the horizontal direction ($\varphi = 90^\circ$). **c)** The conceptual workflow of the polarization filter. When the polarization axis of linear polarizer is set to align with the polarization direction of the box region set in (b), it only allows the light of this part to pass and blocks the surrounding beam, producing a box pattern of intensity with vertical polarization direction. This filtered engineered beam provides a spatial selectivity, for example producing **d)** a deformation only to a single micropillar without affecting the others. The strategy can be expanded to more complex cases, such as a periodic configuration with its own directionality and number of reconfigured pillars (e–g) and an arbitrary pattern (h).

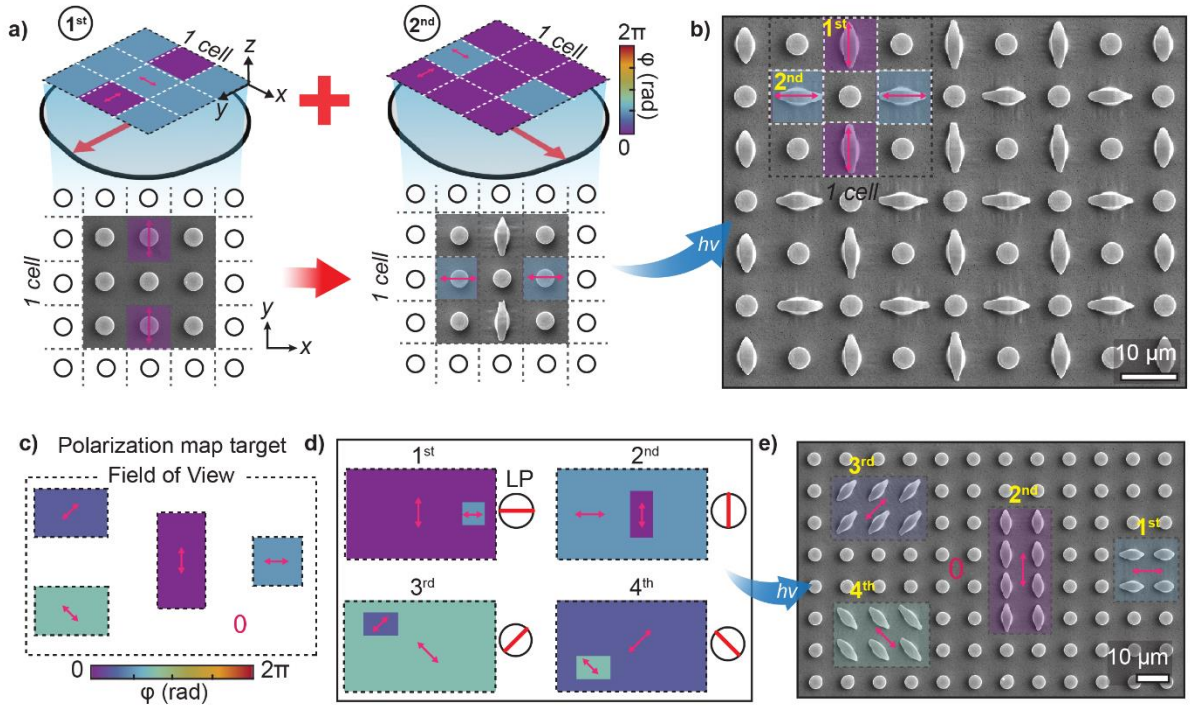


Figure S9. The implementation of the “multi-exposure” approach to achieve complex control of spatial selectivity and local directionality in the final surface configuration. a) The conceptual illustration of the 2-exposure approach to produce a periodic quad-petal formation of anisotropic microstructures. The 1st exposure is performed to generate a unidirectional element of the petals (i.e., the petals along the y-axis) while leaving an azo micropillar in the center of the petal formation unchanged. The 2nd exposure is then performed to add the other unidirectional element of the petals. b) The final morphology of the quad-petal formation of microstructures array. A demonstration of the multi-exposure approach to produce any configuration of anisotropic surface, such as a) 4-box areas with different sizes and local directionalities. To achieve this pattern, the key is to divide the map target into d) four different exposures. Each exposure is designed to convey one element (i.e., one box) of the target map by designing a polarization map that contains only the intended element of the target map and setting the rest of the field of view to orthogonal polarization. The polarization axis of the linear polarization is then adjusted to filter the engineered beam to have only the intended element of the target polarization. e) The final anisotropic surface configuration that matches the target polarization map.

Supplementary note 2: Visualization of light-induced stress pathways using ANSYS software

Primary deformation of azopolymer micropillars follows the major principal direction of the maximum tensile component of the photoinduced stress, which is dictated by the local polarization state of the incident light. In Figure S10, the direction of the x-axis in the local coordinate system for each finite element is shown. It is aligned with the major principal axis of the stress tensor, as the incident light field in this case is linearly polarized, producing a consistent spatial distribution of tensile stress pathways.

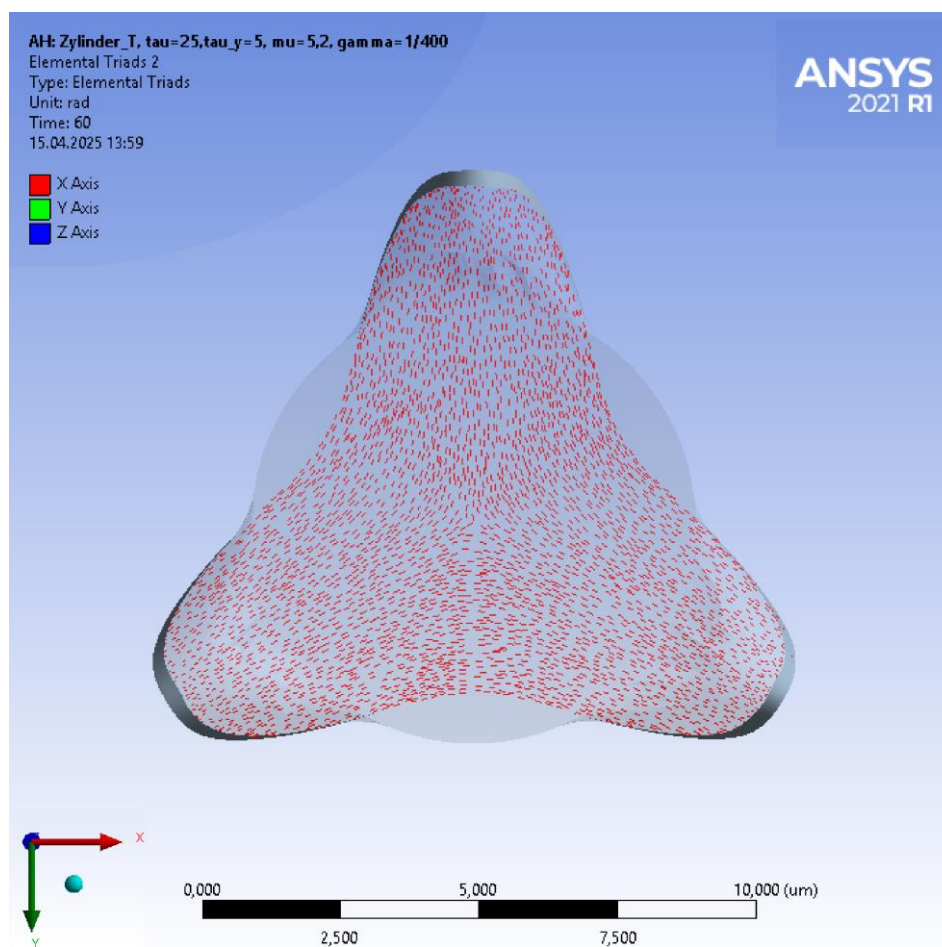


Figure S10. Orientation of the x-axis (red arrows) in the local coordinate system for each finite element, aligned with the major principal axis of the stress tensor. The distribution of axes is shown for the triaxial micropillar system.

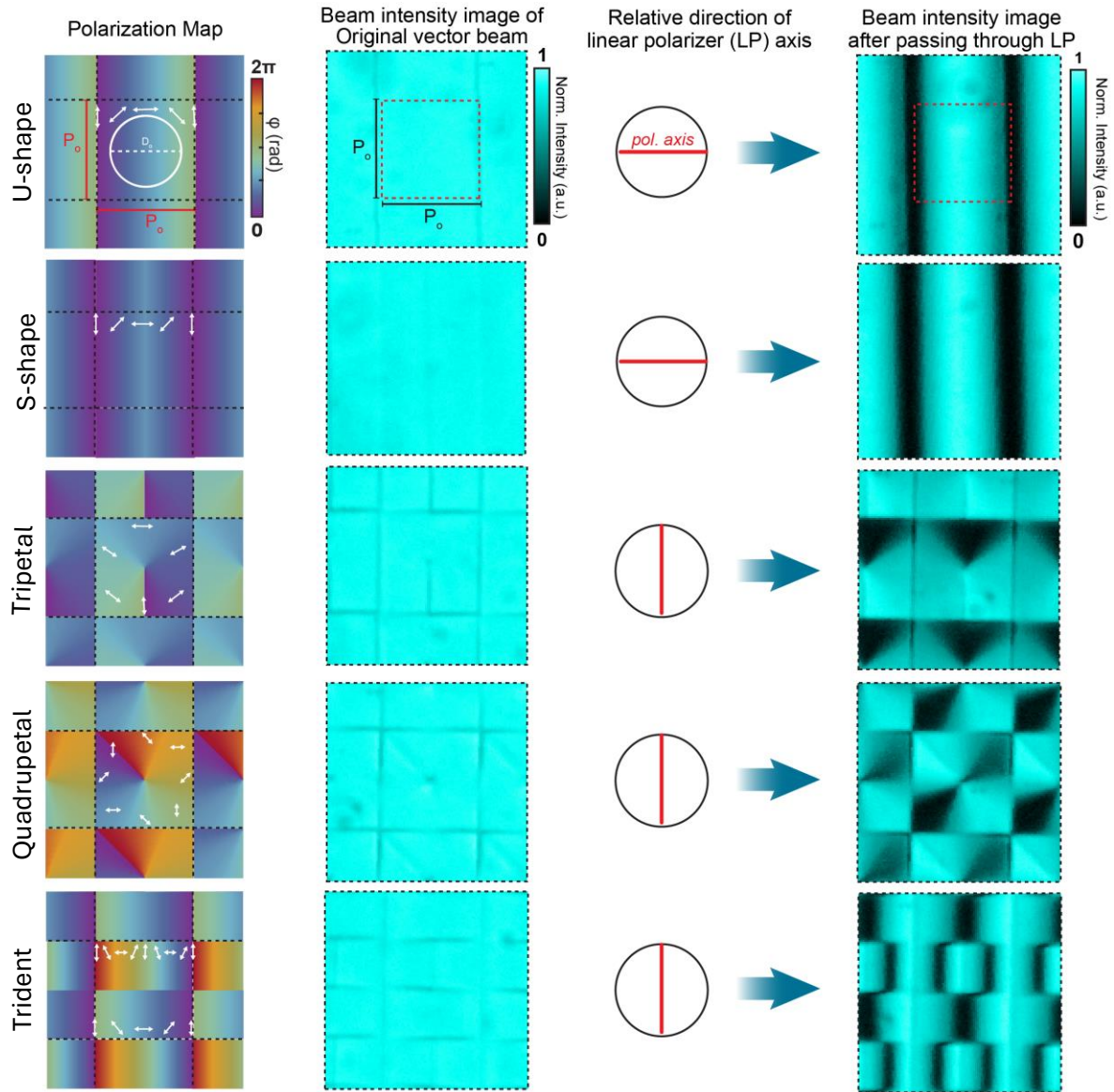


Figure S11. The qualitative characterization of the engineered beam with linear polarization filter. In the left column, the white circular line in the polarization map represents the perimeter of a single micropillar with a diameter of $D_o \approx 6.7 \mu\text{m}$. The white arrows provide visual indicators of the local linear polarization, as programmed by the grayscale value addressed to the SLM. To target a single micropillar in a square array, each polarization map is designed to have an area of $P_o \times P_o \approx 12 \times 12 \mu\text{m}^2$. The characterization was performed with setup shown in Fig. S9 a. A mirror was placed in the sample plane, and subsequently, the CCD camera was utilized to capture an intensity image that was reflected back from the mirror. The original beam intensity images were taken without a linear polarizer (LP) in front of the CCD camera, as shown in the second column. With an LP as oriented in the third column, the resulting CCD images are shown in the fourth column. In order to improve the clarity of the intensity image description, an LED 477 nm (with full width of half maximum = 29 nm) was used as the light source for this experiment.

References

1. Yadav, B.; Domurath, J.; Kim, K.; Lee, S.; Saphiannikova, M., Orientation Approach to Directional Photodeformations in Glassy Side-Chain Azopolymers. *The Journal of Physical Chemistry B* **2019**, *123* (15), 3337-3347.
2. Toshchevikov, V.; Ilnytskyi, J.; Saphiannikova, M., Photoisomerization Kinetics and Mechanical Stress in Azobenzene-Containing Materials. *Journal of Physical Chemistry Letters* **2017**, *8* (5), 1094-1098.
3. Loebner, S.; Lomadze, N.; Kopyshev, A.; Koch, M.; Guskova, O.; Saphiannikova, M.; Santer, S., Light-Induced Deformation of Azobenzene-Containing Colloidal Spheres: Calculation and Measurement of Opto-Mechanical Stresses. *Journal of Physical Chemistry B* **2018**, *122* (6), 2001-2009.
4. Loebner, S.; Yadav, B.; Lomadze, N.; Tverdokhle, N.; Donner, H.; Saphiannikova, M.; Santer, S., Local Direction of Optomechanical Stress in Azobenzene Containing Polymers During Surface Relief Grating Formation. *Macromolecular Materials and Engineering* **2022**, *31* (n/a), 2100990.
5. Yadav, B. Modeling optical inscription of complex surface patterns in azobenzene-containing materials. PhD thesis, TU Dresden, Dresden, 2023.
6. Férec, J. Nonlinear rheology of non-spherical particle suspensions. Habilitation thesis, Université de Bretagne-SUD, Lorient, 2016.

Table S1. The morphological measurements of different polarization map designs of engineered vector beam.

Experiment	Initial Diameter D_o (μm)	Major axis of elongation L (μm)	Minor axis of elongation l (μm)	Related figures in main text
Illumination using engineered vector beam with homogeneous azimuth angle of $\varphi = \pi/4$	4.0 ± 0.1	7.5 ± 0.5	2.5 ± 0.1	Fig. 3e
Illumination using engineered vector beam with checkerboard polarization pattern with periodic distribution of $\varphi_1 = \pi/4$ and $\varphi_2 = 3\pi/4$	4.0 ± 0.1	6.3 ± 0.5	2.7 ± 0.1	Fig. 3f
Gradual rotation of local linear polarization along a row of azopolymer micropillars (1st row)	4.0 ± 0.1	7.6 ± 1.1	2.4 ± 0.2	Fig. S7 (1 st row)
Gradual rotation of local linear polarization along a row of azopolymer micropillars (2 nd row)	4.0 ± 0.1	7.4 ± 1.1	2.6 ± 0.3	Fig. S7 (2 nd row)

Movie S1. VPA dynamic model of morphological evolution of an azopolymer micropillar in the pre-patterned array (top, side, and tilted view). The model incorporates illumination parameters: homogenous linearly polarized light (blue arrow in the movie) at a wavelength of 488 nm applied over a modeled exposure time of 20 minutes. The dynamics were accelerated to reduce computational demand. The colormap represents vertical displacement: red corresponds to the initial state, while dark blue indicates the maximum downward displacement.

Movie S2. VPA dynamic model of morphological evolution of azopolymer micropillars under vectorial illumination. Top and tilted views of the modeled photo-deformation dynamics are shown for two polarization maps resulting in an inverted U-shape, and a chiral S-shape. The model incorporates experimental illumination parameters, including vector beam polarization patterns at a wavelength of 488 nm applied over a modeled exposure time of 60 seconds. The colormap represents vertical displacement: red corresponds to the initial state, while dark blue indicates the maximum downward displacement.

Movie S3. VPA dynamic model of morphological evolution of azopolymer micropillars for vectorial field-guided deformation with multi-axial symmetry. Top and tilted views of the modeled photo-deformation dynamics are shown for three polarization maps resulting in a tripetal-, quadrupetal-, and trident-shape. The model incorporates experimental illumination parameters, including vector beam polarization patterns at a wavelength of 488 nm applied over a modeled exposure time of 45 seconds for the tripetal- and quadrupetal-shape, and 90 seconds for the trident-shape. The colormap represents vertical displacement: red corresponds to the initial state, while dark blue indicates the maximum downward displacement.